Nonlinear Dynamics (2005) 40: 387–417

Mathematical Modeling, Control, Computer Simulation and Laboratory Experiments of a Spatial Servopneumatic Parallel Robot

Part I: Mathematical Models, Controllers, and Computer Simulations

HUBERT HAHN

Laboratory of Control and System Dynamics (RTS), Department of Mechanical Engineering (FB 15), University of Kassel, Möncheberg Strasse 7, 34109 Kassel, Germany (e-mail: hahn@uni-kassel.de; fax: +49-561-804-7768)

(Received: 6 January 2004; accepted: 7 December 2004)

Abstract. In this paper (Part I), the special construction of a controlled parallel structure, called spatial servopneumatic multi-axles test facility (MAP), will be theoretically and numerically investigated and controlled. The investigations include the following steps: (i) design of *mathematical models* of different complexity of both, the *test facility mechanics* in terms of DAEs and ODEs (a multi-body system which contains 13 rigid bodies under spatial motion, connected by joints), and the *servopneumatic actuators*; (ii) construction of different linear and nonlinear (model based) *control algorithms*; (iii) development of a *computer simulation program* of the MAP; and (iv) evaluation of various *computer simulation runs*, obtained by applying different control algorithms and spatial command-input signals. The results show that the *efficiency* of the control algorithms is closely related to their *complexity* and *cost*. In order to check the closeness to reality of the computer simulation results and their benefit for industrial applications, *laboratory experiments* must be formed with the same MAP, the same control algorithms, and applying the same command-input signals which have been used in the computer simulations. These experimental investigations will be presented in Part II of the paper.

Key words: computer simulations, nonlinear control, quality check, servopneumatic actuator configuration, spatial multi-axles test facility, theoretical models

1. Introduction

Spatial feedback controlled parallel structures play an increasing role in various fields of industrial applications such as manipulators, parallel robots (hexapods, delta robots, multi-axles test facilities, and machine tools), in vehicle dynamics, in spacecraft applications, and even in medical engineering. Due to their highly symmetrical structure, *hexapods* (sometimes called *Gough or Stewart platform*, see [1, 2] and the Figures 1a and b) are currently the most popular representatives of parallel structures and parallel robots both in various research projects (see [1–11]) and industrial applications (see [12, 13]). Sometimes spatial parallel robots with more than six actuators (redundant actuator configurations) are required in order to generate, study, and control the constraint forces. Then parallel structures may be chosen that do not completely loose their symmetry by including one or several redundant actuators. Here a robot design, called *multi-axles test facility* (MAP) will be discussed, that can be optionally driven by redundant and non redundant actuator configurations (Figures 1c and 1d). Multi-axles test facilities are extensively used in industry and spacecraft engineering for performing dynamic tests of critical components of machines. Among those, *hydraulic test facilities* are used for testing heavy loads (in earthquake and spacecraft tests) controlled by sinusoidal and by transient test signals (see [14–16]). Transient tests of medium size loads and of small loads are often performed using *servopneumatic test facilities* (see [17–22]). In this paper, a MAP which is driven by *six servo-pneumatic* actuators will be

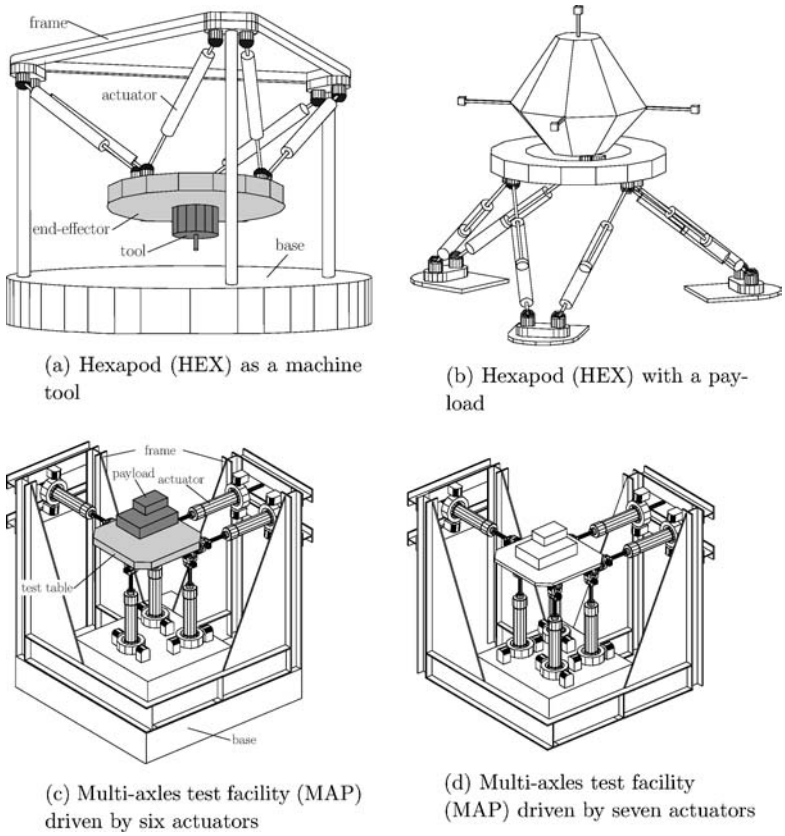

(a) Hexapod (HEX) as a machine tool

(b) Hexapod (HEX) with a payload

(c) Multi-axles test facility (MAP) driven by six actuators

(d) Multi-axles test facility (MAP) driven by seven actuators

Figure 1. Drawings of different parallel robots.

investigated. *Servopneumatic actuators* are low-cost components that operate with the medium gas that is everywhere available (on earth). On the other hand, due to the high compressibility and low viscosity of gas, servo-pneumatic actuators are governed by complex nonlinear model equations (see [17, 23–27]). As a consequence, a MAP which is driven by *servo-pneumatic actuators* is an interesting and useful mechatronic system that requires sophisticated model-based control algorithms. The servopneumatic test facility that will be discussed in this paper has been designed for quite *different purposes*. It serves: (i) as a *manipulator* for precise, rapid, and large spatial motions; (ii) as a *test facility* for spatial vibrations and transient tests of components and systems; (iii) as a flight and *motion simulator*; (iv) as an instrument for experimentally *testing* different redundant and non-redundant *actuator configurations* and sensor or observer configurations; and (v) as a *vehicle* for implementation and experimental *testing* of *different control and identification algorithms* and safety concepts of parallel robots.

The test facility has been developed in several steps: In the *first step*, sophisticated *mathematical models* of both the spatial test facility mechanics and the servo-pneumatic actuators have been derived. Based on analytically computed model parameters of the test facility mechanics and on model parameters of the actuators which were estimated by laboratory experiments, a *computer simulation* of the test facility has been developed in *step two*. In the *third step*, sophisticated linear and nonlinear *control algorithms* were derived based on the model equations of step one. The function and efficiency of the *control algorithms* have been tested in computer simulations. In the *fifth step*, the *test facility has been constructed and built*. Using the procedure of rapid prototyping, the *control algorithms* together with

the required *sensing elements* were *implemented* in the electronic components in *step six*. In the *last step*, a safety system of the test facility has been installed and the *function and quality* of the system have been investigated in *laboratory experiments*. The results obtained by these investigations (mathematical models, computer simulation programs, control and identification algorithms) can be directly applied to quite different types of parallel robots (hexapods, MAPs, machine tools, etc.).

In *Part I* of this paper, the *mathematical models* of the spatial test facility (Section 2) and the *control algorithms* (Section 3) will be presented. The efficiency of the different control loops will be investigated in *computer simulations* (Section 4). In *Part II* of the paper, the *laboratory set-up* of the test facility will be presented (Section 2). Various *laboratory experiments* obtained by applying different command-input signals and nonlinear and linear controllers will be presented in Section 3, where the results obtained by the *laboratory experiments will be compared with the computer simulations*.

2. Model Equations of the Test Facility

In this section, sophisticated model equations of the MAP will be briefly presented which have been used: (i) in the theoretical analysis and design of prototypes of parallel robots and test facilities; (ii) as the basis of computer simulations of the MAP; (iii) as a model hypothesis for identifying the inertia parameters of the MAP; and (iv) as the basis for deriving and implementing real-time model-based controllers. The theoretical models of the MAP include model equations of both the test facility mechanics and the actuators.

2.1. Model Equations of the Test Facility Mechanics

The mechanical model equations describe the spatial motion of 13 rigid bodies (test table, six actuator pistons and six actuator housings), which are driven by six servo-pneumatic actuators (see Figure 2). The

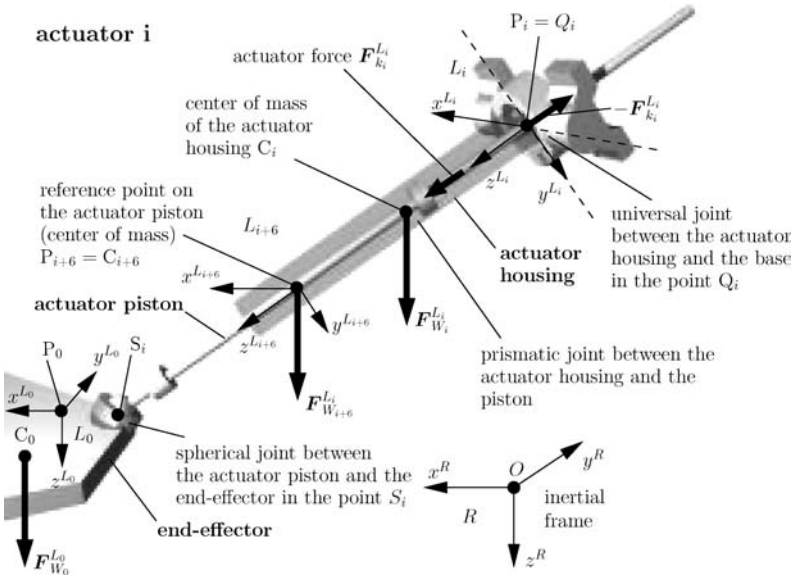

Figure 2. Drawing of an actuator (housing and piston) and of the associated joints.

actuator pistons are connected with the actuator housings by prismatic joints, the actuator housings with the base by universal joints, and the actuator pistons with the test table by spherical joints (Figure 2). The model equations of the 13 rigid bodies of the MAP are derived in detail in Section 8.4 of [29]. They constitute a differential–algebraic system (DAE) of 78 nonlinear *kinematic ODEs* of the first order, 78 nonlinear *kinetic ODEs*, and 72 nonlinear algebraic constrained position equations which describe the joints (see [28] and the Equations 8.154 of [29]). This DAE is projected down to the following system of six nonlinear kinematic ODEs and six nonlinear kinetic ODEs in the six DOFs of the test table of the MAP (see [28] and the Equations 8.227a and 8.227b of [29])

$$\dot{\boldsymbol{p}}_0 = \boldsymbol{T}(\boldsymbol{p}_0) \cdot \boldsymbol{v}_0, \quad \text{(kinematic ODEs)} \tag{1a}$$

$$\boldsymbol{M}(\boldsymbol{p}_0) \cdot \dot{\boldsymbol{v}}_0 = -\boldsymbol{q}_G(\boldsymbol{p}_0,\, \boldsymbol{v}_0) - \boldsymbol{q}_W(\boldsymbol{p}_0) + \boldsymbol{J}_{t6}^{\mathrm{T}}(\boldsymbol{p}_0) \cdot \boldsymbol{F}_k, \quad \text{(kinetic ODEs)} \tag{1b}$$

with the *vector of the Cartesian coordinates* of the *test table*

$$\boldsymbol{p}_0 := \left(\boldsymbol{r}_{PO}^{R\ \mathrm{T}}, \boldsymbol{\eta}_0^{\mathrm{T}}\right)^{\mathrm{T}} = \big(\underbrace{x_{PO}^R,\, y_{PO}^R,\, z_{PO}^R}_{=:(\boldsymbol{r}_{PO}^R)^{\mathrm{T}}},\, \underbrace{\varphi,\, \theta,\, \psi}_{=:\boldsymbol{\eta}_0^{\mathrm{T}}}\big)^{\mathrm{T}}, \tag{2a}$$

with $\boldsymbol{r}_{PO}^R := \boldsymbol{r}_{P_0O}^R = (x_{PO}^R, y_{PO}^R, z_{PO}^R)^{\mathrm{T}}$ as the displacement vector from the origin O of the inertial frame R to the *reference point* P_0 on the test table, represented in R, and with $\boldsymbol{\eta}_0 = (\varphi, \theta, \psi)^{\mathrm{T}}$ as the "orientation vector" of the *Bryant angles* of the frame L_0 (fixed on the test table) with respect to the frame R, the *velocity vector* $\boldsymbol{v}_0 = ((\dot{\boldsymbol{r}}_{P0}^R)^{\mathrm{T}}, (\boldsymbol{\omega}_{L_0R}^{L_0})^{\mathrm{T}} \in \mathbb{R}^6$, with $\dot{\boldsymbol{r}}_{P0}^R := (\dot{x}_{PO}^R, \dot{y}_{PO}^R, \dot{z}_{PO}^R)^{\mathrm{T}}$, $\boldsymbol{\eta}_0 := (\dot{\varphi}, \dot{\theta}, \dot{\psi})^{\mathrm{T}}$, and the angular velocity vector

$$\boldsymbol{\omega}_{L_0R}^{L_0} = \boldsymbol{A}^{L_0R} \cdot \boldsymbol{H}_0^{-1}(\boldsymbol{\eta}_0)\dot{\boldsymbol{\eta}}_0, \tag{2b}$$

with $\boldsymbol{H}_0(\boldsymbol{\eta}_0)$ and $\boldsymbol{T}_0(\boldsymbol{p}_0) = \mathrm{diag}(\mathbf{I}_3, \boldsymbol{H}_0(\boldsymbol{\eta}_0) \cdot \boldsymbol{A}^{RL_0})$ as the kinematic matrices of the test table and $\boldsymbol{A}^{L_0R}$ as the transformation matrix which maps the vector $\boldsymbol{r}$ from the frame R to the frame L_0. The *vector of the forces and torques* due to the *weights* of the 13 bodies is (see (8.228c) of [29])

$$\begin{aligned}\boldsymbol{q}_W(\boldsymbol{p}_0) := -\boldsymbol{f}_0(\boldsymbol{p}_0) - \sum_{i=1}^{6} \Bigg\{ & \boldsymbol{J}_{r_i}^{\mathrm{T}}(\boldsymbol{p}_0) \cdot \tilde{\boldsymbol{P}}_r(z_i) \cdot z_{C_iP_i}^{L_i} \cdot \boldsymbol{A}^{L_iR}(\boldsymbol{p}_0) \cdot \boldsymbol{P}_r(z_i) \cdot m_i \\ & + \begin{bmatrix} \mathbf{I}_3 \\ \tilde{\boldsymbol{r}}_{S_iP_0}^{L_0} \cdot \boldsymbol{A}^{L_0R}(\boldsymbol{p}_0) \end{bmatrix} \cdot \boldsymbol{P}_r(z_i) \cdot m_{i+6} \Bigg\} \cdot g,\end{aligned} \tag{2c}$$

with m_i as the mass of body i ($i = 1, \ldots, 13$), z_i as the displacement coordinate of the actuator i, $\boldsymbol{P}_r(z_i)$ as the abbreviation of the unit vector $(0, 0, 1)^{\mathrm{T}}$, $\boldsymbol{f}_0(\boldsymbol{p}_0)$ as the vector of the external forces and torques which act on the body 13 (end effector, $i = 13$), and with "$\sim$" as the tilde operator which stands for the vector product (for example $\tilde{\boldsymbol{r}} \cdot \boldsymbol{\omega} = \boldsymbol{r} \times \boldsymbol{\omega}$). The matrices $\boldsymbol{J}_{r_i}^{\mathrm{T}}(\boldsymbol{p}_0)$ and $\boldsymbol{J}_{t6}(\boldsymbol{p}_0)$ are the Jacobian matrices of the inverse kinematic relations of the robot (see Comment 1). The *generalized mass matrix* of the 13 rigid bodies is (see (8.228a) of [29])

$$\begin{aligned}\boldsymbol{M}(\boldsymbol{p}_0) := \boldsymbol{M}_0(\boldsymbol{p}_0) + \sum_{i=1}^{6} \left\{\boldsymbol{J}_{r_i}^{\mathrm{T}}(\boldsymbol{p}_0) \cdot \left(\boldsymbol{J}_{P_i}^{L_i} + \boldsymbol{J}_{C_{i+6}}^{L_{i+6}}\right) \cdot \boldsymbol{J}_{r_i}(\boldsymbol{p}_0)\right\} + \boldsymbol{J}_{t_6}^{\mathrm{T}}(\boldsymbol{p}_0) \cdot \boldsymbol{M}_k \cdot \boldsymbol{J}_{t_6}(\boldsymbol{p}_0) \\ - \sum_{i=1}^{6} \left\{ \begin{bmatrix} \mathbf{I}_3 \\ \tilde{\boldsymbol{r}}_{S_iP_0}^{L_0} \cdot \boldsymbol{A}^{L_0R}(\boldsymbol{p}_0) \end{bmatrix} \cdot m_{i+6} \cdot \boldsymbol{A}^{RL_i}(\boldsymbol{p}_0) \cdot \tilde{\boldsymbol{P}}_r(z_i) \cdot \bar{t}_{t_i}(\boldsymbol{p}_0) \cdot \boldsymbol{J}_{r_i}(\boldsymbol{p}_0) \right\}\end{aligned} \tag{2d}$$

with $\boldsymbol{M}_0(\boldsymbol{p}_0) \in \mathbb{R}^{6,6}$ as the generalized mass matrix of the end effector, $\boldsymbol{M}_k = \text{diag}(m_7, \ldots, m_{12})$, and $\boldsymbol{J}_{P_i}^{L_i}$ and $\boldsymbol{J}_{C_{i+6}}^{L_{i+6}}$ as the inertia matrices of the housing and piston of the actuator i. The *vector of the centrifugal forces and gyroscopic terms* is (see (8.228b) of [29])

$$\begin{aligned}
\boldsymbol{q}_G(\boldsymbol{p}_0, \boldsymbol{v}_0) := {} & \boldsymbol{J}_{t_6}^{\mathrm{T}}(\boldsymbol{p}_0) \cdot \boldsymbol{M}_k \cdot \dot{\boldsymbol{J}}_{t6}(\boldsymbol{p}_0, \boldsymbol{v}_0) \cdot \boldsymbol{v}_0 - \boldsymbol{q}_{G_0}(\boldsymbol{p}_0, \boldsymbol{v}_0) \\
& + \sum_{i=1}^{6} \left\{ \boldsymbol{J}_{r_i}^{\mathrm{T}} \cdot \left(\boldsymbol{J}_{P_i}^{L_i} + \boldsymbol{J}_{C_{i+6}}^{L_{i+6}} \right) \cdot \dot{\boldsymbol{J}}_{r_i}(\boldsymbol{p}_0, \boldsymbol{v}_0) \right. \\
& \left. + \boldsymbol{J}_{r_i}^{\mathrm{T}}(\boldsymbol{p}_0) \cdot \widetilde{(\boldsymbol{J}_{r_i}(\boldsymbol{p}_0) \cdot \boldsymbol{v}_0)} \cdot \left(\boldsymbol{J}_{P_i}^{L_i} + \boldsymbol{J}_{C_{i+6}}^{L_{i+6}} \right) \cdot \boldsymbol{J}_{r_i}(\boldsymbol{p}_0) \right\} \cdot \boldsymbol{v}_0 \\
& + \sum_{i=1}^{6} \left\{ \begin{bmatrix} \mathbf{I}_3 \\ \tilde{\boldsymbol{r}}_{S_i P_0}^{L_0} \cdot \boldsymbol{A}^{L_0 R}(\boldsymbol{p}_0) \end{bmatrix} \cdot m_{i+6} \cdot \boldsymbol{A}^{R L_i}(\boldsymbol{p}_0) \cdot \left\{ \widetilde{(\boldsymbol{J}_{r_i}(\boldsymbol{p}_0) \cdot \boldsymbol{v}_0)} \right. \right. \\
& \quad \cdot \left(\boldsymbol{P}_r(z_i) \cdot \boldsymbol{P}_r^{\mathrm{T}}(z_i) \cdot \boldsymbol{A}^{L_i R}(\boldsymbol{p}_0) \cdot \left[\mathbf{I}_3, \; - \boldsymbol{A}^{R L_0}(\boldsymbol{p}_0) \cdot \tilde{\boldsymbol{r}}_{S_i P_0}^{L_0} \right] \right. \\
& \left. + \tilde{\boldsymbol{P}}_r(z_i) \cdot \bar{l}_{t_i}(\boldsymbol{p}_0) \cdot \boldsymbol{J}_{r_i}(\boldsymbol{p}_0) \right) + \tilde{\boldsymbol{P}}_r(z_i) \cdot \left(\boldsymbol{P}_r^{\mathrm{T}}(z_i) \cdot \boldsymbol{A}^{L_i R}(\boldsymbol{p}_0) \right. \\
& \quad \left. \left. \left. \cdot \left[\mathbf{I}_3, \; - \boldsymbol{A}^{R L_0}(\boldsymbol{p}_0) \cdot \tilde{\boldsymbol{r}}_{S_i P_0}^{L_0} \right] \cdot \boldsymbol{v}_0 \cdot \boldsymbol{J}_{r_i}(\boldsymbol{p}_0) + \bar{l}_{t_i}(\boldsymbol{p}_0) \cdot \dot{\boldsymbol{J}}_{r_i}(\boldsymbol{p}_0) \right) \right\} \right\} \cdot \boldsymbol{v}_0, \qquad \text{(2e)}
\end{aligned}$$

with $\boldsymbol{q}_{G_0}(\boldsymbol{p}_0, \boldsymbol{v}_0)$ as the centrifugal forces and gyroscopic terms of the end effector. The vector of the actuator forces and torques is

$$\boldsymbol{F}_k = (\boldsymbol{A}_k \cdot \boldsymbol{p}_L - \boldsymbol{D}_k \cdot \boldsymbol{J}_{t6}(\boldsymbol{p}_0) \cdot \boldsymbol{v}_0). \qquad \text{(2f)}$$

$\boldsymbol{A}_k \cdot \boldsymbol{p}_L$ is the vector of the *actuator forces*, $\boldsymbol{A}_k := \text{diag}(A_{k1}, \ldots, A_{k6}) \in \mathbb{R}^{6,6}$ the matrix of the *actuator piston areas*, $\boldsymbol{p}_L := (p_{L1}, \ldots, p_{L6})^{\mathrm{T}} \in \mathbb{R}^6$ the vector of the *pressure differences* in the *actuator chambers*, and $\boldsymbol{F}_D(\boldsymbol{p}_1, \boldsymbol{v}_1) := \boldsymbol{D}_k \cdot \dot{\boldsymbol{z}}_k = \boldsymbol{D}_k \cdot \boldsymbol{J}_{t6}(\boldsymbol{p}_1) \cdot \boldsymbol{v}_0 \in \mathbb{R}^6$ the vector of the *damping forces* of the *actuators* (see (6.28) and (6.29) of [29]), with $\boldsymbol{z}_k$ as the vector of the *actuator displacements*, and $\boldsymbol{D}_k := \text{diag}(d_{k1}, \ldots, d_{k6}) \in \mathbb{R}^{6,6}$ as the matrix of the *damping coefficients* of the actuators.

Comment 1 (The inverse and direct kinematics of the MAP)**.** *In the model equations of both the robot mechanics and the actuators, mappings will be used which transform the displacements of the actuators* ($\boldsymbol{z}_k$) *into the DOFs of the test table* ($\boldsymbol{p}_0$)*, and vice versa. The first mapping which is sometimes called the inverse kinematic relation of the MAP will be abbreviated as (see (6.23)–(6.25g) of [29]):*

$$\boldsymbol{z}_k = \boldsymbol{t}_t(\boldsymbol{p}_0) \quad \textit{together with} \quad \dot{\boldsymbol{z}}_k = \frac{\partial \boldsymbol{t}_t}{\partial \boldsymbol{p}_0} \cdot \boldsymbol{T}_0(\boldsymbol{p}_0) \cdot \boldsymbol{v}_0 =: \boldsymbol{J}_{t6}(\boldsymbol{p}_0) \cdot \boldsymbol{v}_0 \qquad \text{(3a)}$$

with $\boldsymbol{z}_k := (z_{k_1}, \ldots, z_{k_6})^{\mathrm{T}}$, z_{k_i} *as the displacement of the actuator* i*, and with* $\boldsymbol{J}_{t6}(\boldsymbol{p}_0)$ *as the Jacobian matrix of the inverse kinematic relations of the robot. This mapping is represented by an analytic expression. The inverse relation of (3a)*

$$\boldsymbol{p}_0 = \boldsymbol{t}_t^{-1}(\boldsymbol{z}_k) \quad \textit{and} \quad \boldsymbol{v}_0 = \boldsymbol{T}_0^{-1}(\boldsymbol{p}_0) \cdot \left(\frac{\partial \boldsymbol{t}_t}{\partial \boldsymbol{p}_0} \right)^{-1} \cdot \dot{\boldsymbol{z}}_k \qquad \text{(3b)}$$

is called the direct kinematic relation of the MAP. This relation can usually only be computed numerically. In the model equations, the following variables will also be used: $\bar{l}_{t_i} := t_{t_i} - |\boldsymbol{r}|_{PS_i}$ *with* $|\boldsymbol{r}|_{PS_i}$ *as the constant distance of the actuator piston* i *from its attachment point on the base.*

The orientation of the actuator i is (see (8.181b), (8.185), and (8.187) of [29]):

$$\boldsymbol{\eta}_i = \boldsymbol{t}_{r_i}(\boldsymbol{p}_0) \quad \text{with} \quad \dot{\boldsymbol{\eta}}_i = \frac{\mathrm{d}}{\mathrm{d}t}(\boldsymbol{t}_{r_i}(\boldsymbol{p}_0)) = \frac{\partial \boldsymbol{t}_{r_i}}{\partial \boldsymbol{p}_0} \cdot \boldsymbol{T}_0(\boldsymbol{p}_0) \cdot \boldsymbol{v}_0, \tag{3c}$$

and

$$\begin{aligned} &\boldsymbol{\omega}_{L_i R}^{L_i} = \boldsymbol{A}^{L_i R} \cdot \boldsymbol{H}_i^{-1} \cdot \frac{\partial \boldsymbol{t}_{r_i}(\boldsymbol{p}_0)}{\partial \boldsymbol{p}_0} \cdot \boldsymbol{T}_0(\boldsymbol{p}_0) \cdot \boldsymbol{v}_0 =: \boldsymbol{J}_{r_i}(\boldsymbol{p}_0) \cdot \boldsymbol{v}_0 \quad \textit{with} \\ &\boldsymbol{J}_{r_i}(\boldsymbol{p}_0) := \boldsymbol{A}^{L_i R} \cdot \boldsymbol{H}_i^{-1} \cdot \frac{\partial \boldsymbol{t}_{r_i}(\boldsymbol{p}_0)}{\partial \boldsymbol{p}_0} \cdot \boldsymbol{T}_0(\boldsymbol{p}_0) \in \mathbb{R}^{3,6}. \end{aligned} \tag{3d}$$

The *mechanical model equations* (1) may be written in the form (see (8.227) and (6.30) of [29])

$$\dot{\boldsymbol{p}}_0 = \boldsymbol{T}_0(\boldsymbol{p}_0) \cdot \boldsymbol{v}_0, \tag{4a}$$

$$\dot{\boldsymbol{v}}_0 = \boldsymbol{a}_m(\boldsymbol{p}_0, \boldsymbol{v}_0) + \boldsymbol{b}_m(\boldsymbol{p}_0) \cdot \boldsymbol{p}_L \tag{4b}$$

with

$$\boldsymbol{a}_m(\boldsymbol{p}_0, \boldsymbol{v}_0) := \boldsymbol{M}^{-1}(\boldsymbol{p}_0) \cdot \left[-\boldsymbol{q}_G(\boldsymbol{v}_0, \boldsymbol{p}_0) - \boldsymbol{q}_W(\boldsymbol{p}_0) - \boldsymbol{J}_{t_6}^{\mathrm{T}}(\boldsymbol{p}_0) \cdot \boldsymbol{D}_k \cdot \boldsymbol{J}_{t_6}(\boldsymbol{p}_0) \cdot \boldsymbol{v}_0 \right] \in \mathbb{R}^6 \tag{4c}$$

and

$$\boldsymbol{b}_m(\boldsymbol{p}_0) := \boldsymbol{M}^{-1}(\boldsymbol{p}_0) \cdot \boldsymbol{J}_{t_6}^{\mathrm{T}}(\boldsymbol{p}_0) \cdot \boldsymbol{A}_k \in \mathbb{R}^{6,6}. \tag{4d}$$

These nonlinear mechanics equations (NM) may be compactly written in the *nonlinear state-space form*:

$$\dot{\boldsymbol{x}}_M = \boldsymbol{a}_M(\boldsymbol{x}_M) + \boldsymbol{b}_M(\boldsymbol{x}_M) \cdot \boldsymbol{u}_M \tag{5a}$$

with

$$\boldsymbol{x}_M := \left(\boldsymbol{p}_0^{\mathrm{T}},\ \boldsymbol{v}_0^{\mathrm{T}}\right)^{\mathrm{T}} \in \mathbb{R}^{12} \qquad \text{as the } \textit{state vector} \tag{5b}$$

and

$$\boldsymbol{u}_M = \boldsymbol{p}_L \in \mathbb{R}^6 \qquad \text{as the } \textit{input vector}, \tag{5c}$$

and with

$$\boldsymbol{a}_M(\boldsymbol{x}_M) := \begin{pmatrix} \boldsymbol{T}_0(\boldsymbol{p}_0) \cdot \boldsymbol{v}_0 \\ \boldsymbol{a}_m(\boldsymbol{p}_0, \boldsymbol{v}_0) \end{pmatrix} \in \mathbb{R}^{12} \quad \text{and} \quad \boldsymbol{b}_M(\boldsymbol{x}_M) := \begin{pmatrix} \boldsymbol{0}_{6,6} \\ \boldsymbol{b}_m(\boldsymbol{p}_0) \end{pmatrix} \in \mathbb{R}^{12,6}. \tag{5d}$$

The model Equations (1a) and (1b) will be abbreviated by the letters *NM*, subsequently. They are the basis for all *computer simulations* of the MAP. They are also used in the *parameter identification* of

some model parameters and as the basis of the *computed-force controller CF–NM* (see Section 3). Assuming *massless actuators*, and inserting

$$m_i = m_{i+6} \approx 0, \quad i = 1, \ldots, 6 \tag{6a}$$

and

$$\boldsymbol{J}_{P_i}^{L_i} = \boldsymbol{J}_{C_{i+6}}^{L_{i+6}} \approx \boldsymbol{0}_{3,3} \quad \text{for} \quad i = 1, \ldots, 6 \tag{6b}$$

into the model Equations (1a)–(2f), provides the *simplified ODEs of the single-mass parallel robot*:

$$\dot{\boldsymbol{p}}_0 = \boldsymbol{T}_0(\boldsymbol{p}_0) \cdot \boldsymbol{v}_0 \tag{7a}$$

$$\boldsymbol{M}_0(\boldsymbol{p}_0) \cdot \dot{\boldsymbol{v}}_0 = \boldsymbol{q}_{G_0}(\boldsymbol{p}_0, \boldsymbol{v}_0) + \boldsymbol{f}_0(\boldsymbol{p}_0) + \boldsymbol{J}_{t_6}^{\mathrm{T}}(\boldsymbol{p}_0) \cdot \boldsymbol{F}_k. \tag{7b}$$

These model equations, called reduced mechanics (RM), serve as the basis of the *model-based controllers* (*CF–RM*, *FL–RMNP*) of Section 3. Replacing in $\boldsymbol{a}_m$ (4c) and $\boldsymbol{b}_m$ (4d) the functions $\boldsymbol{M}$, $\boldsymbol{q}_G$, and $\boldsymbol{q}_W$ by the functions $\boldsymbol{M}_0$ (2d), $-\boldsymbol{q}_{G_0}$ (2e), and $-\boldsymbol{f}_0$ (2c), respectively, yields the model equations of the reduced mechanical system (7a), (7b) which will be written in the form

$$\dot{\boldsymbol{x}}_M = \boldsymbol{a}_R(\boldsymbol{x}_M) + \boldsymbol{b}_R(\boldsymbol{x}_M) \cdot \boldsymbol{u}_M \tag{8a}$$

with

$$\boldsymbol{a}_R(\boldsymbol{x}_M) := \begin{pmatrix} \boldsymbol{T}_0(\boldsymbol{p}_0) \cdot \boldsymbol{v}_0 \\ \boldsymbol{a}_r(\boldsymbol{p}_0, \boldsymbol{v}_0) \end{pmatrix} \in \mathbb{R}^{12} \quad \text{and} \quad \boldsymbol{b}_R(\boldsymbol{x}_M) := \begin{pmatrix} \boldsymbol{0}_{6,6} \\ \boldsymbol{b}_r(\boldsymbol{p}_0) \end{pmatrix} \in \mathbb{R}^{12,6}, \tag{8b}$$

$$\boldsymbol{a}_r(\boldsymbol{p}_0, \boldsymbol{v}_0) := \boldsymbol{M}_0^{-1}(\boldsymbol{p}_0) \cdot \left[+\boldsymbol{q}_{G_0}(\boldsymbol{v}_0, \boldsymbol{p}_0) + \boldsymbol{f}_0(\boldsymbol{p}_0) + \boldsymbol{J}_{t_6}^{\mathrm{T}}(\boldsymbol{p}_0) \cdot \boldsymbol{D}_k \cdot \boldsymbol{J}_{t_6}(\boldsymbol{p}_0) \cdot \boldsymbol{v}_0 \right] \in \mathbb{R}^6 \tag{8c}$$

and

$$\boldsymbol{b}_r(\boldsymbol{p}_0) := \boldsymbol{M}_0^{-1}(\boldsymbol{p}_0) \cdot \boldsymbol{J}_{t_6}^{\mathrm{T}}(\boldsymbol{p}_0) \cdot \boldsymbol{A}_k \in \mathbb{R}^{6,6}. \tag{8d}$$

The reduced nonlinear model Equations (7) are formally much less complex than the model Equations (4) or (5), due to the fact that they only include a single rigid body (the end effector) and no joint models. As a consequence, the control algorithms which take into account the model Equations (7) are much simpler than those which are based on the model Equations (4).

Linearization of the reduced mechanical model Equations (8a) for a constant input vector $\boldsymbol{u}_c := \boldsymbol{p}_{Lc}$ in an associated equilibrium point $\boldsymbol{x}_{Mc} = (\boldsymbol{p}_{0c}^{\mathrm{T}}, \boldsymbol{0}_6^{\mathrm{T}})^{\mathrm{T}}$ provides the reduced *linear model equations* of the MAP mechanics

$$\dot{\bar{\boldsymbol{x}}}_M = \boldsymbol{A}_R(\boldsymbol{x}_{Mc}, \boldsymbol{u}_{Mc}) \cdot \bar{\boldsymbol{x}}_M + \boldsymbol{B}_R(\boldsymbol{x}_{Mc}, \boldsymbol{u}_{Mc}) \cdot \bar{\boldsymbol{u}}_M \tag{9}$$

of the *single mass model* (8a) with

$$\bar{\boldsymbol{x}}_M := \boldsymbol{x}_M - \boldsymbol{x}_{Mc} \in \mathbb{R}^{12} \quad \text{and} \quad \bar{\boldsymbol{u}}_M := \boldsymbol{u}_M - \boldsymbol{u}_{Mc} \in \mathbb{R}^6$$

and the matrices $\boldsymbol{A}_R(\boldsymbol{x}_{Mc}, \boldsymbol{u}_{Mc}) \in \mathbb{R}^{12,12}$ and $\boldsymbol{B}_R(\boldsymbol{x}_{Mc}, \boldsymbol{u}_{Mc}) \in \mathbb{R}^{12,6}$, as shown in Section 6.2.5 of [29]. These model equations will be abbreviated by the linear mechanics (LM) expression.

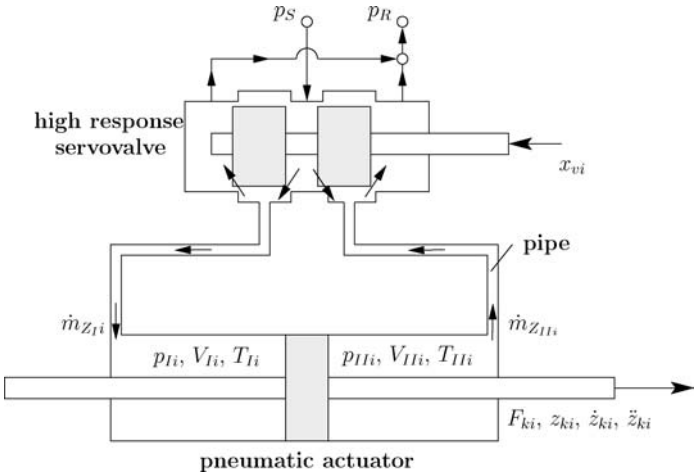

Figure 3. Schematic drawing of a servo-pneumatic actuator.

2.2. Model Equations of the Servopneumatic Actuators

Each actuator includes a torque motor (which moves the piston of the servo-valve), a servo-valve with the control edges, and a cylinder (see Figure 3). Subsequently, it will be assumed (i) that the torque motor is an ideal linear component (its transfer function has no poles and zeros), (ii) that the valve mechanics may be described by linear model equations of the second order, (iii) that the leakage and bypass flows are assumed to be zero, and (iv) that the control edges of the valves are considered to have zero overlappings. The mechanical behavior of each of the six valves will be modeled both by the trivial model equations, trivial valve model (TV)

$$x_{vi} = k_{vi} \cdot u_{vi}, \quad i = 1, \ldots, 6, \tag{10a}$$

and by the linear ODEs LV (Linear Valve Model) (see [17, 23–27])

$$\ddot{x}_{vi} + 2 \cdot \zeta_{vi} \cdot \omega_{vi} \cdot \dot{x}_{vi} + \omega_{vi}^2 \cdot x_{vi} = k_{vi} \cdot \omega_{vi}^2 \cdot u_i, \quad i = 1, \ldots, 6 \tag{10b}$$

with the

- servo-valve piston displacements x_{vi} (Figure 3),
- servo-valve gain factors k_{vi},
- servo-valve damping factors ζ_{vi}, and
- servo-valve frequencies ω_{vi}.

The model equation (10b) of the servo-valve includes both the static and dynamic behavior of the servo-valve piston, whereas the model equation (10a) only represents its static behavior. The *pressure evolution* in the actuator chambers (p_{Ii}, p_{IIi}) is modeled by the two nonlinear differential Equations (11a) and (11b), assuming isentropic processes in the actuator chambers, constant temperatures T_S and T_R of the gas, and constant system pressures p_S and p_R of the fluid power supply:

$$\dot{p}_{Ii} = a'_{AIi}(\dot{m}_{zIi}(p_{Ii}, x_{vi}),\ p_{Ii},\ \dot{z}_{ki}) \tag{11a}$$

$$\dot{p}_{IIi} = a'_{AIIi}(\dot{m}_{zIIi}(p_{IIi}, x_{vi}),\ p_{IIi},\ \dot{z}_{ki}) \tag{11b}$$

with

$$a'_{AIi} = \frac{\kappa \cdot [R \cdot T_{Ii} \cdot \dot{m}_{ZIi}(p_{Ii}, x_{vi}) - A_k \cdot \dot{z}_{ki} \cdot p_{Ii}]}{A_k \cdot z_{ki} + V_{0Ii}}, \tag{11c}$$

$$a'_{AIIi} = \frac{\kappa \cdot [R \cdot T_{IIi} \cdot \dot{m}_{ZIIi}(p_{IIi}, x_{vi}) + A_k \cdot \dot{z}_{ki} \cdot p_{IIi}]}{A_k \cdot z_{ki} - V_{0IIi}}, \tag{11d}$$

and the

- actuator piston areas $A_k = A_{ki}$ $(i = 1, \ldots, 6)$,
- viscous damping coefficients d_{ki} of the actuator i,
- actuator piston displacements z_{ki},
- pressures p_{Ii} and p_{IIi} in the actuator chambers Ii and IIi,
- initial volumes V_{01i} and V_{0IIi} of the actuator chambers Ii and IIi,
- gas constant R, and
- adiabatic exponent κ.

The mass flows $\dot{m}_{ZIi}$ into and $\dot{m}_{ZIIi}$ out of the actuator chambers are

$$\begin{aligned}\dot{m}_{ZIi}(p_{Ii}, x_{vi}) = &-\alpha_{D1i} \cdot A_{1i}(x_{vi}) \cdot \psi\left(\frac{p_R}{p_{Ii}}\right) \cdot p_{Ii} \cdot \sqrt{\frac{2}{R \cdot T_{Ii}}} \\ &+ \alpha_{D2i} \cdot A_{2i}(x_{vi}) \cdot \psi\left(\frac{p_{Ii}}{p_S}\right) \cdot p_S \cdot \sqrt{\frac{2}{R \cdot T_S}}\end{aligned} \tag{12a}$$

and

$$\begin{aligned}\dot{m}_{ZIIi}(p_{IIi}, x_{vi}) = &\alpha_{D3i} \cdot A_{3i}(x_{vi}) \cdot \psi\left(\frac{p_{IIi}}{p_S}\right) \cdot p_S \cdot \sqrt{\frac{2}{R \cdot T_S}} \\ &- \alpha_{D4i} \cdot A_{4i} \cdot \psi\left(\frac{p_R}{p_{IIi}}\right) \cdot p_{IIi} \cdot \sqrt{\frac{2}{R \cdot T_{II}}}.\end{aligned} \tag{12b}$$

- The valve orifice areas A_{1i} to A_{4i}, which depend on the servo-valve piston displacements x_{vi} are:

$$A_{ni} = \begin{cases} \pi \cdot d_{ni} \cdot x_{vi} & \text{for } x_{vi} \geq 0 \\ 0 & \text{for } x_{vi} < 0 \end{cases} \quad \text{for} \quad n = 2, 4, \tag{12c}$$

$$A_{ni} = \begin{cases} -\pi \cdot d_{ni} \cdot x_{vi} & \text{for } x_{vi} \leq 0 \\ 0 & \text{for } x_{vi} > 0 \end{cases} \quad \text{for} \quad n = 1, 3\,. \tag{12d}$$

- The flow coefficients of the valve orifices are α_{D1i} to α_{D4i}.
- The nonlinear flow functions $\psi(\frac{p_v}{p_\mu})$ of the control edges which depend on the pressure ratio $\frac{p_v}{p_\mu}$ and on the critical pressure ratio p_{crit} are:

$$\psi\left(\frac{p_v}{p_\mu}\right) = \begin{cases} \psi_0 \cdot \sqrt{1 - \left(\frac{\frac{p_v}{p_\mu} - p_{\text{crit}}}{1 - p_{\text{crit}}}\right)^2} & \text{for } \frac{p_v}{p_\mu} \geq p_{\text{crit}} \\ \psi_0 \cdot & \text{for } \frac{p_v}{p_\mu} < p_{\text{crit}} \end{cases}, \tag{12e}$$

where $v = R, Ii, IIi,\ \mu = S, Ii, IIi\ ; v \neq \mu\ ;\ i = 1, \ldots, 6.$

- T_{Ii} and T_{IIi} are the fluid temperatures in the actuator chambers Ii and IIi.

Then the model Equations (11a) and (11b) can be written in the *bilinear form*

$$\dot{p}_{Ii} = a_{AIi}(\dot{z}_{ki},\, z_{ki},\, p_{Ii}) + b_{AIi}(z_{ki},\, p_{Ii}) \cdot x_{vi}, \tag{13a}$$

$$\dot{p}_{Ii} = a_{AIIi}(\dot{z}_{ki},\, z_{ki},\, p_{IIi}) + b_{AIIi}(z_{ki},\, p_{IIi}) \cdot x_{vi} \tag{13b}$$

with

$$a_{AIi} := \frac{-\kappa \cdot A_k \cdot \dot{z}_{ki} \cdot p_{Ii}}{A_k \cdot z_{ki} + V_{0Ii}}, \quad b_{AIi} := \frac{\kappa \cdot R \cdot T_{Ii} \cdot \dot{m}'_{zIi}(p_{Ii})}{A_k \cdot z_{ki} + V_{0Ii}}, \tag{13c}$$

$$a_{AIIi} := \frac{+\kappa \cdot A_k \cdot \dot{z}_{ki} \cdot p_{IIi}}{A_k \cdot z_{ki} - V_{0IIi}}, \quad b_{AIIi} := \frac{\kappa \cdot R \cdot T_{IIi} \cdot \dot{m}'_{zIIi}(p_{IIi})}{A_k \cdot z_{ki} - V_{0IIi}}, \tag{13d}$$

$$\dot{m}'_{zIi} := \dot{m}_{zIi}/x_{vi} \quad \text{and} \quad \dot{m}'_{zIIi} := \dot{m}_{zIIi}/x_{vi}.$$

Collecting the model Equations (10b), (13a), and (13b) of the six actuators, yields the following overall actuator model (which will be abbreviated by the letters NP (nonlinear pneumatics):

$$\dot{\boldsymbol{x}}_A = \boldsymbol{a}_A(\boldsymbol{x}) + \boldsymbol{b}_A(\boldsymbol{x}) \cdot \boldsymbol{u}_A \quad \text{and} \quad \boldsymbol{y}_A = \boldsymbol{c}_A(\boldsymbol{x}_A), \tag{14a}$$

with

$$\begin{aligned}
\boldsymbol{x}_A &:= \left(\boldsymbol{p}_I^{\mathrm{T}}, \boldsymbol{p}_{II}^{\mathrm{T}}, \boldsymbol{x}_v^{\mathrm{T}}, \dot{\boldsymbol{x}}_v^{\mathrm{T}}\right)^{\mathrm{T}} \in \mathbb{R}^{24}, \quad \boldsymbol{x} := \left(\boldsymbol{x}_M^{\mathrm{T}}, \boldsymbol{x}_A^{\mathrm{T}}\right)^{\mathrm{T}} \in \mathbb{R}^{36}, \\
\boldsymbol{p}_I &:= (p_{I1}, \ldots, p_{I6})^{\mathrm{T}}, \quad \boldsymbol{p}_{II} := (p_{II1}, \ldots, p_{II6})^{\mathrm{T}}, \quad \boldsymbol{p}_L := \boldsymbol{p}_I - \boldsymbol{p}_{II}, \\
\boldsymbol{x}_v &:= (x_{v1}, \ldots, x_{v6})^{\mathrm{T}}, \quad \boldsymbol{u}_A := (u_{v1}, \ldots, u_{v6})^{\mathrm{T}}, \text{ and} \\
\boldsymbol{a}_A(x) &:= \left[\boldsymbol{a}_{AI}^{\mathrm{T}}(\boldsymbol{x}_1, \boldsymbol{x}_2, \boldsymbol{p}_I) + [\boldsymbol{b}_{AI}(\dot{\boldsymbol{m}}'_{zI}, \boldsymbol{z}_k) \cdot \boldsymbol{x}_v]^{\mathrm{T}}, \quad \boldsymbol{a}_{AII}^{\mathrm{T}}(\boldsymbol{x}_1, \boldsymbol{x}_2, \boldsymbol{p}_{II})\right. \\
&\quad \left. + [\boldsymbol{b}_{AII}(\dot{\boldsymbol{m}}'_{zII}, \boldsymbol{z}_k) \cdot \boldsymbol{x}_v]^{\mathrm{T}}, \dot{\boldsymbol{x}}_v^{\mathrm{T}}, -\left(\boldsymbol{\omega}_v^2 \cdot \boldsymbol{x}_v\right)^{\mathrm{T}} - 2 \cdot (\boldsymbol{\zeta}_v \cdot \boldsymbol{\omega}_v \cdot \dot{\boldsymbol{x}}_v)^{\mathrm{T}}\right]^{\mathrm{T}} \in \mathbb{R}^{24},
\end{aligned} \tag{14b}$$

with

$$\begin{aligned}
\boldsymbol{z}_k &= \boldsymbol{t}_t(\boldsymbol{p}_0), \quad \boldsymbol{x}_M = (\boldsymbol{p}_0^{\mathrm{T}}, \boldsymbol{v}_0^{\mathrm{T}}), \\
\boldsymbol{a}_{AI} &= (a_{AI1}, \ldots, a_{AI6})^{\mathrm{T}}, \quad \boldsymbol{a}_{AII} = (a_{AII1}, \ldots, a_{AII6})^{\mathrm{T}}, \\
\boldsymbol{\omega}_v &:= \mathrm{diag}(\omega_{v1}, \ldots, \omega_{v6})^{\mathrm{T}}, \quad \boldsymbol{\omega}_v^2 = \boldsymbol{\omega}_v \cdot \boldsymbol{\omega}_v, \\
\boldsymbol{\zeta}_v &:= \mathrm{diag}(\zeta_{v1}, \ldots, \zeta_{v6}) \quad \text{and} \quad \boldsymbol{z}_k := (z_{k1}, \ldots, z_{k6}), \\
\boldsymbol{b}_{AI} &= \mathrm{diag}(\boldsymbol{b}_{AI1}, \ldots, \boldsymbol{b}_{AI6}), \quad \boldsymbol{b}_{AII} = (\boldsymbol{b}_{AII1}, \ldots, \boldsymbol{b}_{AII6}) \in \mathbb{R}^{6,6}, \\
\dot{\boldsymbol{m}}'_{zI} &:= (\dot{m}'_{zI1}, \ldots, \dot{m}'_{zI6})^{\mathrm{T}}, \quad \dot{\boldsymbol{m}}'_{zII} := (\dot{m}'_{zII1}, \ldots, \dot{m}'_{zII6})^{\mathrm{T}},
\end{aligned} \tag{14c}$$

and

$$\boldsymbol{b}_A(\boldsymbol{x}_A) := \left[\boldsymbol{0}_{6,6},\, \boldsymbol{0}_{6,6},\, \boldsymbol{0}_{6,6},\, \left(\boldsymbol{k}_v \cdot \boldsymbol{\omega}_v^2\right)^{\mathrm{T}}\right]^{\mathrm{T}} \in \mathbb{R}^{24,6} \tag{14d}$$

with

$$\boldsymbol{k}_v = \mathrm{diag}(k_{v1}, \ldots, k_{v6}). \tag{14e}$$

It should be mentioned that the function $\boldsymbol{a}_A(\boldsymbol{x})$ includes compositions of the functions $\boldsymbol{a}_{AI}(z_k, \dot{z}_k, \boldsymbol{p}_I)$, $\boldsymbol{a}_{AII}(z_k, \dot{z}_k, \boldsymbol{p}_{II})$ and $\boldsymbol{b}_{AI}(\boldsymbol{m}'_{zI}, z_k)$, $\boldsymbol{b}_{AII}(\boldsymbol{m}'_{zII}, z_k)$ with the *inverse kinematic relations* (3a). By introducing certain symmetry assumptions (see [23]), the two pressure evolution Equations (13a) and (13b) in the variables $\boldsymbol{p}_I$ and $\boldsymbol{p}_{II}$, respectively, can be combined to a single vector equation in the variable $\boldsymbol{p}_L := \boldsymbol{p}_I - \boldsymbol{p}_{II}$. Linearization of this reduced model equation of the actuators in a suitable operation point $(\boldsymbol{x}_{Ac}, \boldsymbol{u}_{vc})$ yields, together with the trivial valve equation (10a), the reduced *linear* actuator model

$$\dot{\bar{\boldsymbol{x}}}_A := \boldsymbol{A}_{AR}(\boldsymbol{x}_{Ac}, \boldsymbol{u}_{vc}) \cdot \bar{\boldsymbol{x}}_A + \boldsymbol{B}_{AR}(\boldsymbol{x}_{Ac}, \boldsymbol{u}_{vc}) \cdot \bar{\boldsymbol{u}}_v \tag{15}$$

with

$$\bar{\boldsymbol{x}}_A := \boldsymbol{x}_A - \boldsymbol{x}_{Ac} = \bar{\boldsymbol{p}}_L = \boldsymbol{p}_L - \boldsymbol{p}_{Lc} \in \mathbb{R}^6 \quad \text{and} \quad \bar{\boldsymbol{u}}_v := \boldsymbol{u}_v - \boldsymbol{u}_{vc} \in \mathbb{R}^6 \quad \text{and} \quad \boldsymbol{A}_{AR},\ \boldsymbol{B}_{AR} \in \mathbb{R}^{6,6}.$$

This linear actuator model, linear pneumatics will be abbreviated as (*LP*).

The *nonlinear* model Equations NM (5a) (test facility mechanics) and NP (14a) (actuators) provide, together with the connection equations of these two equations

$$\boldsymbol{u}_M = \boldsymbol{p}_L := \boldsymbol{p}_I - \boldsymbol{p}_{II} \quad \text{and} \quad z_k = \boldsymbol{t}_t(\boldsymbol{p}_0) \tag{16}$$

the nonlinear *state-space equations of the test facility* (MAP)

$$\dot{\boldsymbol{x}} = \boldsymbol{a}(\boldsymbol{x}) + \boldsymbol{b}(\boldsymbol{x}) \cdot \boldsymbol{u} \tag{17a}$$

with

$$\begin{aligned}
\boldsymbol{x} &= \left(\boldsymbol{x}_1^{\mathrm{T}}, \boldsymbol{x}_2^{\mathrm{T}}, \boldsymbol{x}_3^{\mathrm{T}}, \boldsymbol{x}_4^{\mathrm{T}}, \boldsymbol{x}_5^{\mathrm{T}}, \boldsymbol{x}_6^{\mathrm{T}}\right)^{\mathrm{T}} := \big(\underbrace{\boldsymbol{p}_0^{\mathrm{T}}, \boldsymbol{v}_0^{\mathrm{T}}}_{=\boldsymbol{x}_M^{\mathrm{T}}}, \underbrace{\boldsymbol{p}_I^{\mathrm{T}}, \boldsymbol{p}_{II}^{\mathrm{T}}, \boldsymbol{x}_v^{\mathrm{T}}, \dot{\boldsymbol{x}}_v^{\mathrm{T}}}_{=\boldsymbol{x}_A^{\mathrm{T}}}\big)^{\mathrm{T}} \in \mathbb{R}^{36}, \\
\boldsymbol{u} &:= \boldsymbol{u}_A := (u_{v1}, \ldots, u_{v6})^{\mathrm{T}}, \\
\boldsymbol{a}(\boldsymbol{x}) &= \left(\boldsymbol{a}_M^{\mathrm{T}}(\boldsymbol{x}_M), \boldsymbol{a}_A^{\mathrm{T}}(\boldsymbol{x}_A)\right)^{\mathrm{T}} \\
&= \big[(\boldsymbol{T}_0(\boldsymbol{p}_0) \cdot \boldsymbol{v}_0)^{\mathrm{T}}, \boldsymbol{a}_m^{\mathrm{T}}(\boldsymbol{p}_0, \boldsymbol{v}_0) + [\boldsymbol{b}_m(\boldsymbol{p}_0) \cdot (\boldsymbol{p}_I - \boldsymbol{p}_{II})]^{\mathrm{T}}, \\
&\quad \boldsymbol{a}_{AI}^{\mathrm{T}}(\dot{z}_k, z_k, \boldsymbol{p}_I) + [\boldsymbol{b}_{AI}(\dot{\boldsymbol{m}}'_{zI}, z_k) \cdot \boldsymbol{x}_v]^{\mathrm{T}}, \boldsymbol{a}_{AII}^{\mathrm{T}}(\dot{z}_k, z_k, \boldsymbol{p}_{II}) + [\boldsymbol{b}_{AII}(\dot{\boldsymbol{m}}'_{zII}, z_k) \cdot \boldsymbol{x}_v]^{\mathrm{T}}, \dot{\boldsymbol{x}}_v^{\mathrm{T}}, \\
&\quad -\left(\boldsymbol{\omega}_v^2 \cdot \boldsymbol{x}_v\right)^{\mathrm{T}} - 2 \cdot (\boldsymbol{\zeta}_v \cdot \boldsymbol{\omega}_v \cdot \dot{\boldsymbol{x}}_v)^{\mathrm{T}}\big]^{\mathrm{T}} \in \mathbb{R}^{36},
\end{aligned} \tag{17b}$$

and

$$\boldsymbol{b}(\boldsymbol{x}) = \left[\boldsymbol{0}_{6,6}, \boldsymbol{0}_{6,6}, \boldsymbol{0}_{6,6}, \boldsymbol{0}_{6,6}, \boldsymbol{0}_{6,6}, \left(\boldsymbol{k}_v \cdot \boldsymbol{\omega}_v^2\right)^{\mathrm{T}}\right]^{\mathrm{T}} \in \mathbb{R}^{36,6}.$$

The model Equations (17a) will be abbreviated by the expression *NMNPLV* (*NM n*onlinear *m*echanics of the 13 mass model, *NP n*onlinear *p*neumatic model of the actuators, and *LV l*inear *v*alve mechanics). This model serves as the basis of the *computer simulations*. The block diagram of these model equations is drawn in Figure 4a.

Replacing the servo-valve equations LV (10b) by the equations TV (10a), and the model equations of the 13-mass model (1a,1b) or (5a) by the single mass model equations RM (8a), provides the model

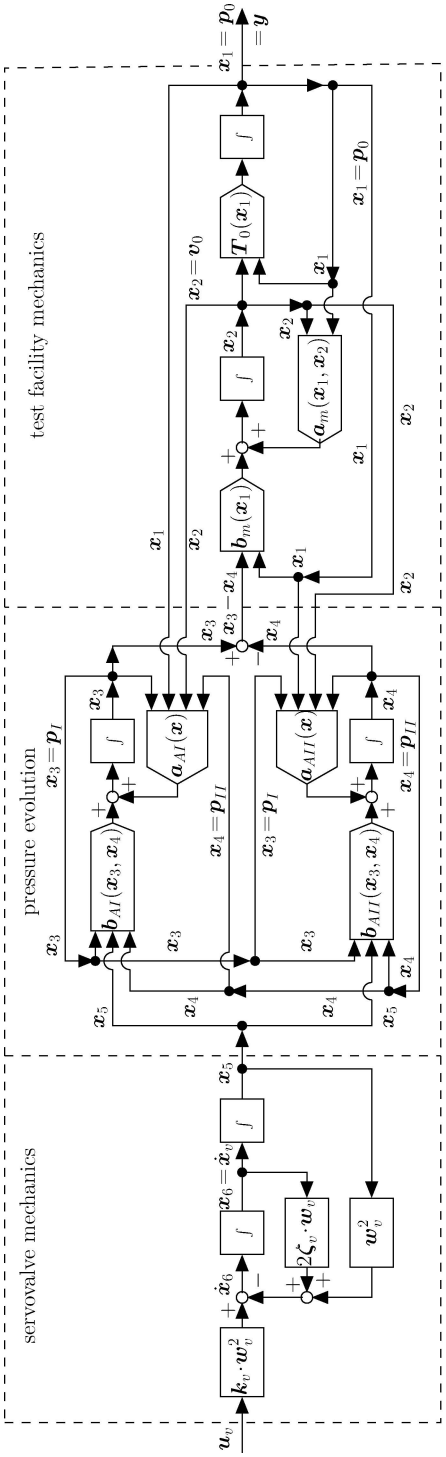

(a) Block diagram of the test facility model NMNPLV (17a)

(b) Block diagram of the control loop with the plant model (17a), and the controllers (20) and (3a)

Figure 4. Block diagrams of the test facility model NMNPLV (17a) (a), and of the control loop which includes the plant model Equations (17a), the linear MS controller (20), and the nonlinear kinematic decoupling prefilter (3a) (b).

equations *RMNP* (reduced mechanics) which obviously follow from the model Equations NMNPLV (17a).

These nonlinear model equations (RMNP) are

$$\begin{aligned}
\dot{\boldsymbol{x}}_1 &= \boldsymbol{T}_0(\boldsymbol{x}_1) \cdot \boldsymbol{x}_2 \\
\dot{\boldsymbol{x}}_2 &= \boldsymbol{a}_r(\boldsymbol{x}_1, \boldsymbol{x}_2) + \boldsymbol{b}_r(\boldsymbol{x}_1) \cdot (\boldsymbol{x}_3 - \boldsymbol{x}_4) \\
\dot{\boldsymbol{x}}_3 &= \boldsymbol{a}_{AI}(\boldsymbol{x}) + \boldsymbol{b}_{AI}(\boldsymbol{x}) \cdot \boldsymbol{k}_v \cdot \boldsymbol{u}_v \\
\dot{\boldsymbol{x}}_4 &= \boldsymbol{a}_{AII}(\boldsymbol{x}) + \boldsymbol{b}_{AII}(\boldsymbol{x}) \cdot \boldsymbol{k}_v \cdot \boldsymbol{u}_v,
\end{aligned} \tag{18a}$$

or abbreviated as

$$\dot{\boldsymbol{x}} = \boldsymbol{a}(\boldsymbol{x}) + \boldsymbol{b}(\boldsymbol{x}) \cdot \boldsymbol{u} \tag{18b}$$

with the new vectors:

$$\begin{aligned}
\boldsymbol{x} &= \left(\boldsymbol{x}_1^{\mathrm{T}}, \boldsymbol{x}_2^{\mathrm{T}}, \boldsymbol{x}_3^{\mathrm{T}}, \boldsymbol{x}_4^{\mathrm{T}}\right)^{\mathrm{T}} := \left(\boldsymbol{p}_0^{\mathrm{T}}, \boldsymbol{v}_0^{\mathrm{T}}, \boldsymbol{p}_I^{\mathrm{T}}, \boldsymbol{p}_{II}^{\mathrm{T}}\right)^{\mathrm{T}} \in \mathbb{R}^{24}, \\
\boldsymbol{u} &:= \boldsymbol{u}_A := (u_{v1}, \ldots, u_{v6})^{\mathrm{T}},
\end{aligned}$$

(where the vector components $\boldsymbol{x}_5$ and $\boldsymbol{x}_6$ are dropped), and the new operators

$$\begin{aligned}
\boldsymbol{a}(\boldsymbol{x}) = \big[&(\boldsymbol{T}_0(\boldsymbol{p}_0) \cdot \boldsymbol{v}_0)^{\mathrm{T}}, \boldsymbol{a}_r^{\mathrm{T}}(\boldsymbol{p}_0, \boldsymbol{v}_0) + [\boldsymbol{b}_r(\boldsymbol{p}_0) \cdot (\boldsymbol{p}_I - \boldsymbol{p}_{II})]^{\mathrm{T}}, \\
&\boldsymbol{a}_{AI}^{\mathrm{T}}(\dot{z}_k, z_k, \boldsymbol{p}_I), \boldsymbol{a}_{AII}^{\mathrm{T}}(\dot{z}_k, z_k, \boldsymbol{p}_{II})\big]^{\mathrm{T}} \in \mathbb{R}^{24}
\end{aligned} \tag{18c}$$

and

$$\boldsymbol{b}(\boldsymbol{x}) = [\boldsymbol{0}_{6,6}, \boldsymbol{0}_{6,6}, (\boldsymbol{b}_{AI}(\dot{\boldsymbol{m}}'_{zI}, z_k) \cdot \boldsymbol{k}_v)^{\mathrm{T}}, (\boldsymbol{b}_{AII}(\dot{\boldsymbol{m}}'_{zII}, z_k) \cdot \boldsymbol{k}_v)^{\mathrm{T}}]^{\mathrm{T}} \in \mathbb{R}^{24,6}.$$

The model equations RMNP (18) serve as the basis of the feedback linearization controller FL–RMNP.

Combining the LM Equations (9) (test facility mechanics) and LP (15) (actuators) by means of the connection equation

$$\bar{\boldsymbol{u}}_M := \bar{\boldsymbol{x}}_A = \bar{\boldsymbol{p}}_L, \tag{19a}$$

yields the *linear model equations* of the test facility (abbreviated by the letters *LMLP*):

$$\dot{\bar{\boldsymbol{x}}} = \boldsymbol{A}(\boldsymbol{x}_c, \boldsymbol{u}_{vc}) \cdot \bar{\boldsymbol{x}} + \boldsymbol{B}(\boldsymbol{x}_c, \boldsymbol{u}_{vc}) \cdot \bar{\boldsymbol{u}}_v \tag{19b}$$

with the state vector

$$\bar{\boldsymbol{x}} := \left(\bar{\boldsymbol{x}}_1^{\mathrm{T}}, \bar{\boldsymbol{x}}_2^{\mathrm{T}}, \bar{\boldsymbol{x}}_3^{\mathrm{T}}\right)^{\mathrm{T}} = \left(\bar{\boldsymbol{p}}_0^{\mathrm{T}}, \bar{\boldsymbol{v}}_0^{\mathrm{T}}, \bar{\boldsymbol{p}}_L^{\mathrm{T}}\right)^{\mathrm{T}} \in \mathbb{R}^{18}, \quad \bar{\boldsymbol{u}}_v \in \mathbb{R}^6 \tag{19c}$$

and

$$\boldsymbol{A} = \begin{pmatrix} \boldsymbol{A}_R, \boldsymbol{B}_R \\ \boldsymbol{0}_{6,12}, \boldsymbol{A}_{AR} \end{pmatrix} \in \mathbb{R}^{18,18}, \quad \boldsymbol{B} = \begin{pmatrix} \boldsymbol{0}_{12,6} \\ \boldsymbol{B}_{AR} \end{pmatrix} \in \mathbb{R}^{18,6}.$$

Table 1. Collection of the subsystem models of the robot.

Collected subsystem models of the robot	Abbreviation	Equations
Nonlinear 13-mass model	NM	(5)
Nonlinear single-mass model	RM	(7)
Linear single-mass model	LM	(9)
Linear static servo-valve model	TV	(10a)
Linear dynamic servo-valve model	LV	(10b)
Nonlinear pressure evolution equations	NP	(13) and (14)
Linear reduced pressure evolution equations	LP	(15)

These model equations serve as the basis of the feedback linearization controller *FL-LMLP* in Section 3. The *gain scheduling controller GS-LMLP* has been derived by using the model equations LMLP with the operating point coordinates $\boldsymbol{p}_{0c}$ and $\boldsymbol{p}_{Lc}$ as the *gain-scheduling variables* (see [30]). The different robot models of the preceding discussion are collected in Table 1.

3. Control Algorithms

Control algorithms can be roughly classified by the amount of information about the plant they use. A controller may have at its disposal: (i) information of the *state* of the plant obtained by sensing elements (*state feedback controller*); (ii) information about the *disturbances* (*disturbance rejection controller*); (iii) information about the *structure and the model parameters* of the plant which are included in the control algorithm (*model-based controller*); and (iv) information about the *uncertainty* about the correct state vector, the disturbances, the model equations, and the model parameters (*robust controller*). Here different controllers of the categories (i) (*state feedback controllers*) and (iii) (*model-based controllers*) will be applied to the MAP. Some of the controllers which have been used in the computer simulations and laboratory experiments will now be briefly introduced, starting with the simple controllers (which use a minimum information of the MAP) to the complexer controllers (which include more and more information about the MAP). Each of the controllers includes the complete information of the *inverse kinematics* (3a) of the MAP, either as a nonlinear *kinematic decoupling prefilter* (PD), multi-sensor (MS), and *PVG (pole-placement) controllers*) or as a part of the nonlinear compensation and decoupling controllers (the computed-force (CF), gain-scheduling (GS), and feedback-linearization (FL) controllers). Apart from the kinematic decoupling prefilter, the first three controllers are basiquely single-axles controllers: The simplest control concept includes for each of the six actuators a simple linear PD controller together with the measured actuator displacements ($\boldsymbol{z}_k \in \mathbb{R}^6$) as the feedback signals. The linear *multi-sensor controller* (*MS*) has the same structure as the PD controller, but uses, in addition to $\boldsymbol{z}_k$, also the measured actuator velocities $\dot{\boldsymbol{z}}_k$ and accelerations $\ddot{\boldsymbol{z}}_k$, and a linear differentiating prefilter. The model equations of the *MS controller* are

$$\boldsymbol{u} = \boldsymbol{K}_P \cdot \boldsymbol{K}_M \cdot \left[\left(\boldsymbol{z}_{kd}^{\mathrm{T}}, \dot{\boldsymbol{z}}_{kd}^{\mathrm{T}}, \ddot{\boldsymbol{z}}_{kd}^{\mathrm{T}} \right) - \left(\boldsymbol{z}_k^{\mathrm{T}}, \dot{\boldsymbol{z}}_k^{\mathrm{T}}, \ddot{\boldsymbol{z}}_k^{\mathrm{T}} \right) \right] \tag{20}$$

with the desired actuator displacements $\boldsymbol{z}_{kd} \in \mathbb{R}^6$, and with the matrices of the controller coefficients $\boldsymbol{K}_P \in \mathbb{R}^{6,18}$ and $\boldsymbol{K}_M \in \mathbb{R}^{18,18}$. The block diagram of the MS controller is shown in Figure 4b. The linear *pole-placement controller* (*PVG*) has the same structure as the MS controller. It includes the additionally

measured feedback signals $\boldsymbol{x}_v$ (servo-valve piston displacements) and $\boldsymbol{p}_L := \boldsymbol{p}_I - \boldsymbol{p}_{II} = \boldsymbol{u}_M$ (pressure differences in the actuator chambers), and the signals $\hat{\boldsymbol{x}}_v$ obtained by a linear observer of the valve mechanics.

The nonlinear *computed-force controller decouples* and *compensates* the *kinematics* and the *kinetics* of the robot *mechanics* by means of its nonlinear *inverse model* (see [20–22, 31–33]). It does not compensate the actuator dynamics. This controller *provides*, in addition, tracking control by using a linear pole-placement controller together with a linear prefilter. The *nonlinear decoupling* and *compensation controller* has been designed based on the *nonlinear* model equations of the robot mechanics NM (5a):

$$\begin{pmatrix} \dot{\boldsymbol{x}}_1 \\ \dot{\boldsymbol{x}}_2 \end{pmatrix} = \begin{pmatrix} \boldsymbol{T}_0(\boldsymbol{x}_1) \cdot \boldsymbol{x}_2 \\ \boldsymbol{a}_m(\boldsymbol{x}_M) \end{pmatrix} + \begin{pmatrix} \boldsymbol{0}_{6,6} \\ \boldsymbol{b}_m(\boldsymbol{x}_M) \end{pmatrix} \cdot \boldsymbol{u}_M, \tag{21}$$

with the vector of the pressure differences $\boldsymbol{u}_M := \boldsymbol{p}_L$ as the inputs of the robot mechanics. The *CF–NM* controller has been derived in the following *steps*: (i) state space *transformation* into a suitable nonlinear normal form, (ii) design of the *nonlinear decoupling* and *compensation controller*, and (iii) design of a *linear pole-placement controller* and *linear prefilter*. The Steps (i) and (ii) yield the *nonlinear decoupling and compensation controller* (Figure 5a):

$$\boldsymbol{u}_{Md} = \boldsymbol{b}_m^{-1}(\boldsymbol{x}_M) \cdot \boldsymbol{T}_0^{-1}(\boldsymbol{x}_1) \cdot \left[\boldsymbol{u}' - \frac{\mathrm{d}}{\mathrm{d}t}(\boldsymbol{T}_0(\boldsymbol{x}_1)) \cdot \boldsymbol{x}_2 - \boldsymbol{T}_0(\boldsymbol{x}_1) \cdot \boldsymbol{a}_m(\boldsymbol{x}_M) \right]. \tag{22a}$$

Step (iii) provides the *pole-placement controller*

$$\boldsymbol{u}' := \boldsymbol{u}'' - \boldsymbol{K}_2 \cdot \boldsymbol{T}_0(\boldsymbol{x}_1) \cdot \boldsymbol{x}_2 - \boldsymbol{K}_1 \cdot \boldsymbol{x}_1 \tag{22b}$$

and the *linear prefilter*

$$\boldsymbol{u}'' := \ddot{\boldsymbol{x}}_{1d} + \boldsymbol{K}_2 \cdot \dot{\boldsymbol{x}}_{1d} + \boldsymbol{K}_1 \cdot \boldsymbol{x}_{1d} \tag{22c}$$

with the desired vector of the positions/orientations of the end effector $\boldsymbol{x}_{1d}$. The CF–NM controller has been derived by assuming an ideal force (pressure) behavior of the actuators. In order to justify this assumption, the linear pressure controller (see Figure 5a)

$$\boldsymbol{u} = \boldsymbol{k}_p \cdot [\boldsymbol{u}_{Md} - \boldsymbol{p}_L], \quad \boldsymbol{p}_L = \boldsymbol{u}_M \tag{22d}$$

has been included in the control loop. This control concept requires the *mechanical* and *geometrical* parameters of the robot and *measurements* of the *position* and *velocity* of the *end effector* and of the *pressure* differences. The computed force controllers CF–RM and CF–LM are obtained identically by replacing the model equations NM (5) by the model equations RM (8) and LM (9), respectively.

The feedback linearization controller (*FL–RMNP controller*) *compensates* and *decouples* the entire dynamics of the parallel robot (including the *kinetics*, the *kinematics*, and the *pressure evolution* of the MAP) (see [20–22, 31–33]). The design of this controller is based on the model Equations RMNP (18) which include the reduced Equations (7) of the test facility mechanics instead of the extended Equations (5). This controller has been derived by the following steps: (i) computation of the *relative degree* of the model (RMNP), (ii) state space *transformation* into a nonlinear normal form, (iii) design

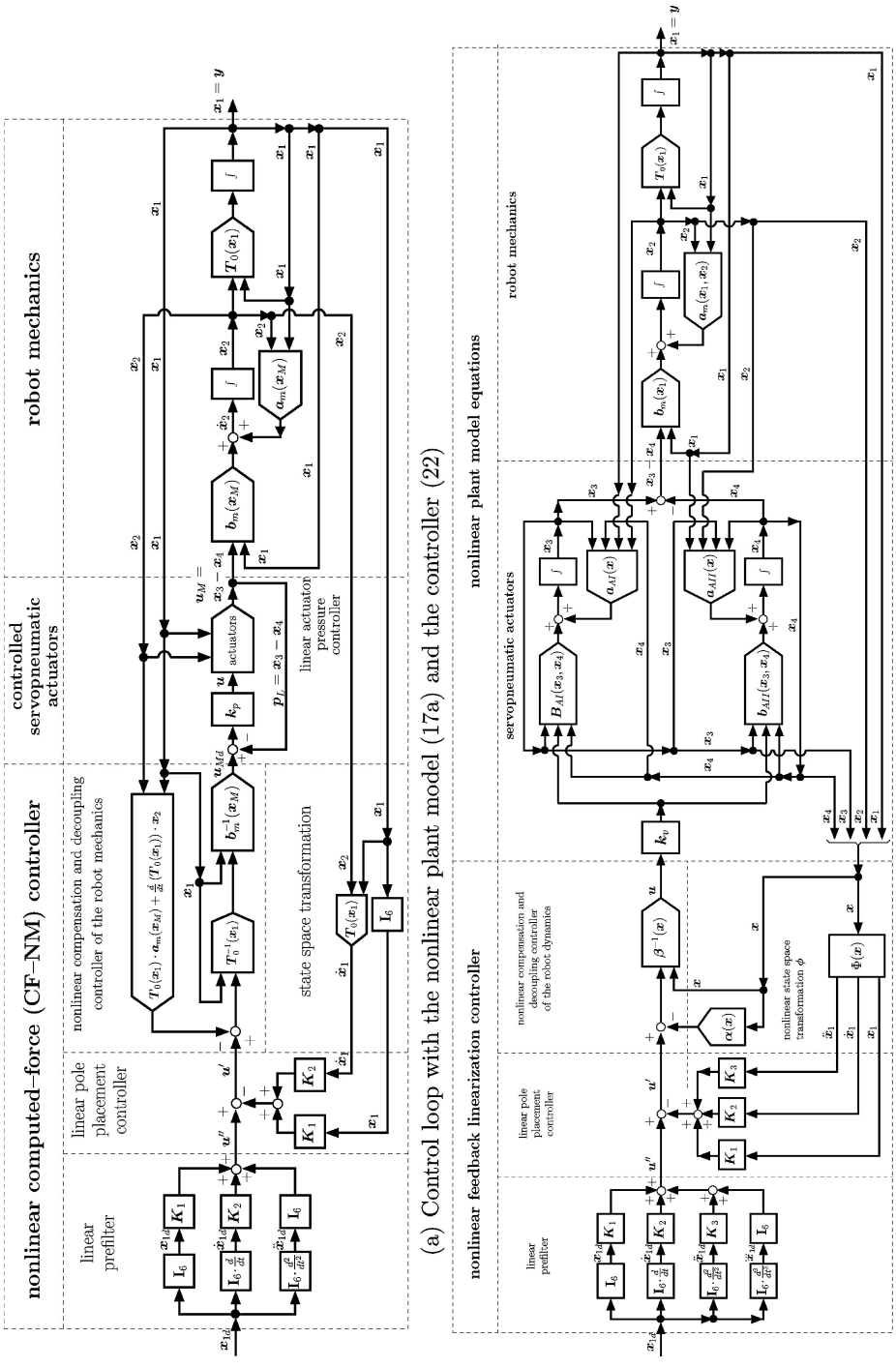

(a) Control loop with the nonlinear plant model (17a) and the controller (22)

(b) Control loop of the plant model NMNPLV (17a) and the nonlinear controller FL-RMNP (23)

Figure 5. Control loops with the nonlinear plant (17a), the nonlinear computed-force controller CF–NM and the linear actuator controllers (22) (a), with the nonlinear feedback i/o-linearization controller FL–RMNP (23) (b).

of the *nonlinear decoupling* and *compensation controller*, and (iv) design of a *linear pole-placement controller* and of a *linear prefilter*. The Step (i) provides the relative degree $r := 18 < 24 = n$ of the plant model equations RMNP (18). The resulting so called internal system of the dimension 6 ($6 = 24 - 18$) has no influence on the system output ($\boldsymbol{y} = \boldsymbol{x}_1$). Laboratory experiments and computer simulations show that this internal system and its zero dynamics are stable. The zero dynamics occurs, because only the *difference pressure* between the two actuator chambers act on the load. The zero dynamics of the robot could be avoided if the pressure of each actuator chamber would be controlled by an individual servo-valve. This solution is too expensive in common applications of servo-drives. The observed stability of the zero dynamics enables the input/output feedback linearization of the nonlinear system (18). The Steps (ii) and (iii) yield the *nonlinear decoupling and compensation controller* (see Figure 5b)

$$\boldsymbol{u} = \boldsymbol{\beta}^{-1}(\boldsymbol{\Phi}(\boldsymbol{x})) \cdot [\boldsymbol{u}' - \boldsymbol{\alpha}(\boldsymbol{\Phi}(\boldsymbol{x}))] \tag{23a}$$

with the vector functions

$$\boldsymbol{\beta}^{-1}(\boldsymbol{\Phi}(\boldsymbol{x})) := \boldsymbol{k}_v^{-1} \cdot [\boldsymbol{b}_{AI}(\boldsymbol{x}_3, \boldsymbol{x}_4) - \boldsymbol{b}_{AII}(\boldsymbol{x}_3, \boldsymbol{x}_4)]^{-1} \cdot \boldsymbol{b}_r^{-1}(\boldsymbol{x}_1) \cdot \boldsymbol{T}_0^{-1}(\boldsymbol{x}_1) \in \mathbb{R}^{6,6} \tag{23b}$$

and

$$\begin{aligned}\boldsymbol{\alpha}(\boldsymbol{\Phi}(\boldsymbol{x})) := {} & \frac{\mathrm{d}^2}{\mathrm{d}t^2}(\boldsymbol{T}_0(\boldsymbol{x}_1)) \cdot \boldsymbol{x}_2 + 2 \cdot \frac{\mathrm{d}}{\mathrm{d}t}(\boldsymbol{T}_0(\boldsymbol{x}_1)) \cdot [\boldsymbol{a}_r(\boldsymbol{x}_1, \boldsymbol{x}_2) + \boldsymbol{b}_r(\boldsymbol{x}_1) \cdot (\boldsymbol{x}_3 - \boldsymbol{x}_4)] + \boldsymbol{T}_0(\boldsymbol{x}_1) \\ & \cdot \left[\frac{\mathrm{d}}{\mathrm{d}t}(\boldsymbol{a}_r(\boldsymbol{x}_1, \boldsymbol{x}_2)) + \frac{\mathrm{d}}{\mathrm{d}t}(\boldsymbol{b}_r(\boldsymbol{x}_1)) \cdot (\boldsymbol{x}_3 - \boldsymbol{x}_4) + \boldsymbol{b}_r(\boldsymbol{x}_1) \cdot (\boldsymbol{a}_{AI}(\boldsymbol{x}) - \boldsymbol{a}_{AII}(\boldsymbol{x}))\right] \in \mathbb{R}^6.\end{aligned} \tag{23c}$$

The step (*iv*) yields the *pole-placement controller*

$$\boldsymbol{u}' := \boldsymbol{u}'' - \boldsymbol{K}_3 \cdot \boldsymbol{\Phi}_3(\boldsymbol{x}) - \boldsymbol{K}_2 \cdot \boldsymbol{\Phi}_2(\boldsymbol{x}) - \boldsymbol{K}_1 \cdot \boldsymbol{x}_1 \tag{23d}$$

and the prefilter

$$\boldsymbol{u}'' := \boldsymbol{K}_3 \cdot \ddot{\boldsymbol{x}}_{1d} + \boldsymbol{K}_2 \cdot \dot{\boldsymbol{x}}_{1d} + \boldsymbol{K}_1 \cdot \boldsymbol{x}_{1d}, \tag{23e}$$

with the components of the nonlinear state-space transformation

$$\begin{aligned}&\boldsymbol{\Phi}(\boldsymbol{x}) = (\Phi_1(\boldsymbol{x}), \Phi_2(\boldsymbol{x}), \Phi_3(\boldsymbol{x}))^{\mathrm{T}} \quad \text{with} \\ &\boldsymbol{x}_1 := \Phi_1(\boldsymbol{x}), \quad \dot{\boldsymbol{x}}_1 := \Phi_2(\boldsymbol{x}) := \boldsymbol{T}_0(\boldsymbol{x}_1) \cdot x_2, \quad \text{and} \\ &\ddot{\boldsymbol{x}}_1 := \Phi_3(\boldsymbol{x}) := \frac{\mathrm{d}}{\mathrm{d}t}(\boldsymbol{T}_0(\boldsymbol{x}_1)) \cdot \boldsymbol{x}_2 + \boldsymbol{T}_0(\boldsymbol{x}_1) \cdot [\boldsymbol{a}_r(\boldsymbol{x}) + \boldsymbol{b}_r(\boldsymbol{x}_1) \cdot (\boldsymbol{x}_3 - \boldsymbol{x}_4)],\end{aligned} \tag{23f}$$

which maps the given plant model equations (RMNP) into the desired nonlinear control canonical form

$$\dot{\boldsymbol{x}}' = \left(\dot{\boldsymbol{x}}_1'^{\mathrm{T}}, \dot{\boldsymbol{x}}_2'^{\mathrm{T}}, \dot{\boldsymbol{x}}_3'^{\mathrm{T}}\right)^{\mathrm{T}} = \boldsymbol{\alpha}(\boldsymbol{x}') + \boldsymbol{\beta}(\boldsymbol{x}') \cdot \boldsymbol{u}, \quad \boldsymbol{x}' = \boldsymbol{\Phi}(\boldsymbol{x}) \tag{24a}$$

Table 2. Subsystem models used in the control algorithms.

Control algorithm	Model equations used
Nonlinear kinematic prefilter	(3a)
Nonlinear computed force (CF–NM)	Nonlinear 13-mass-model (5)
Nonlinear reduced computed force (CF–RM)	Nonlinear single-mass model (8)
Linear compensation controller (CF–LM)	linear single-mass model (9)
Feedback-linearization controller (FL–RMNP)	(8), (14), and (10a)
Linear compensation controller (FL-LMLP)	(9), (15), and (10a)
Gain-scheduling controller (GS-LMLP)	(9), (15), and (10a) with variable operating point coordinates as gain-scheduling variables

with the new state vector

$$\boldsymbol{x}' := \left(\dot{\boldsymbol{x}}_1^{\mathrm{T}}, \dot{\boldsymbol{x}}_2^{\mathrm{T}}, \dot{\boldsymbol{x}}_3^{\mathrm{T}}\right)^{\mathrm{T}} \in \mathbb{R}^{18} . \tag{24b}$$

This enables to derive the controller FL–RMNP (23a). The *gain-scheduling controller* (GS) has been derived along the same line as the above FL controller by using the linear plant model equations LMLP (19b) with the coordinates of the chosen operation point vector $(\boldsymbol{p}_{0c}^{\mathrm{T}}, \boldsymbol{p}_{Lc}^{\mathrm{T}})^{\mathrm{T}}$ as the *gain-scheduling variables* (see [30, 31]). The preceding model-based control algorithms are collected in Table 2.

In consideration of both the *amount of work* to *derive and implement the control algorithms* and the *hardware cost of the controllers and sensors*, the above discussed controllers may be roughly divided into four classes: (i) the PD controller with the kinematic decoupling controller, (ii) the MS and PVG controllers, each with the kinematic decoupling prefilter, (iii) the CF controllers, and (iv) the GS and the FL controllers. The efficiency of these controllers will be investigated by means of computer simulations in the next section of this paper, and by laboratory experiments in Part II of this paper.

4. Computer Simulations

In all of the *computer simulations* presented in this paper, the model equations *NMNPLV* have been used. They include, in addition to the Equations (18), friction models for each actuator (called Stribeck models) and describe the behavior of the multi-axles test facility (MAP) driven by six non-redundant actuators (see Figure 1c). The model equations and control algorithms of the MAP of Figure 1d with eight (redundant) actuators are discussed in [19] for a planar MAP and in [20] for a spatial MAP. The derived algorithms enable to achieve predetermined time histories of some components of the resulting constraint forces/torques. They have been used to prestress the overall system. These rather complex model equations which include the 13-mass model of the robot mechanics (5), the nonlinear extended pressure evolution equations of the actuators (15), together with nonlinear friction models for each of the actuators, and the dynamic linear models (10b) of the servo-valve are the most sophisticated models of the robot which have been derived and applied. The computer simulations of the robot have been extensively used; (i) to find *constructional alternatives* of the laboratory set-up; (ii) to choose a proper layout of the test facility; (iii) to study the dynamic behavior of the test facility both in normal operation and in *limit situations* in order to avoid the risk of its destruction in laboratory experiments; (iv) to check the functioning and efficiency of the different *control algorithms*; (v) to investigate

different configurations of sensing elements and drives; (vi) to check the functioning of the different hardware components in *hardware-in-the-loop simulations*; and (vii) to serve as a helpful instrument for *implementing* the control algorithms in the test facility hardware, using rapid-prototyping techniques.

The computer simulations have been performed using different *command-input signals, control algorithms, sensor configurations, actuator configurations* and *mechanical loads*, and modified *model parameters*: (i) The applied *command-input signals* are modified earthquake signals in three DOFs of the test table, sine-sweep signals in the six DOFs of the test table, spatial and planar motions of the test table on a circle, on the surface of a ball, on the surface of a cylinder, and straight-line motions between the corners of a cube. (ii) The control algorithms which have been tested together with the associated sensing elements are (see Section 3): a *PD-controller*, a *multi-sensor controller (MS)*, a *pole-placement controller (PVG)*, different types of linear and nonlinear *computed force controllers* (CF–LM, CF–RM, CF–NM), gain-scheduling controllers (GS), feedback linearization controllers (FL–LMLP and FL–RMNP), and a sliding-mode controller (SM). The parameters of each of these controllers have been kept constant in all computer simulations and laboratory experiments. (iii) The computer simulations have been performed with different *actuator configurations*: six, seven, and eight actuators. Significant *model parameters* such as the mass and the moments of inertia of the test table and load, the system pressure of the actuators, the upper limit frequency of the servo valves, and the sampling rate of the signals were modified. (iv) The *evaluation criteria* of the controllers were the *effort* and *cost* of the controller design: the *time* needed to derive the analytical model equations, the *complexity (length)* of the model equations, the *computation time* of the control algorithms, the effort to implement the control algorithms (the size of the control algorithms), the *cost of the control hardware* (electronic circuits and sensing elements), and the *quality of the control system* in nominal operation (tracking, stability) and under parameter variations (sensitivity, robustness). Some of the computer simulation results are shown in the Figures 6a–11. The Figures 6a–8b have the following structure: Column 1 includes the command-input signals (desired outputs). The remainder four columns contain the actual outputs (Figures 6a, 7a and 8b) or the output errors defined as the differences between the desired and the actual outputs (Figures 6b, 7b and 8a) obtained by using the PD-, MS-, CF–RM, and FL–RMNP-controllers, each as a representative of one of the four classes of controllers introduced in Section 3. The first six rows of the figures show the time histories of the six DOFs of the test table. The rows 7 to 12 include the associated accelerations. The CPU-time needed by a controller to process the control algorithm has been chosen as a measure of the cost of the controller. It turned out to be proportional to the length (complexity) of the control algorithm and to the amount of work needed to derive the underlying model equations and the model-based controller. It can also (cum grano salis) be considered to be proportional to the cost of the electronic hardware and the sensing elements required by the algorithm. The CPU times are plotted in row 13 of the figures. The last two rows of each figure include two quality indices of the control loops which were computed for each command-input signal, one for judging the quality of the trajectories (DOFs) of the test table, and the other as a quality measure of the associated accelerations. These quality indices are defined by the following expressions:

$$q_x := 6 \cdot \left\{ \sum_{i=1}^{6} \int_0^{t_{\text{end}}} |x_{1id} - x_{1i}| \, \mathrm{d}t \right\}^{-1} \tag{25a}$$

and

$$q_{\ddot{x}} := 6 \cdot \left\{ \sum_{i=1}^{6} \int_0^{t_{\text{end}}} |\ddot{x}_{1id} - \ddot{x}_{1i}| \, \mathrm{d}t \right\}^{-1} \tag{25b}$$

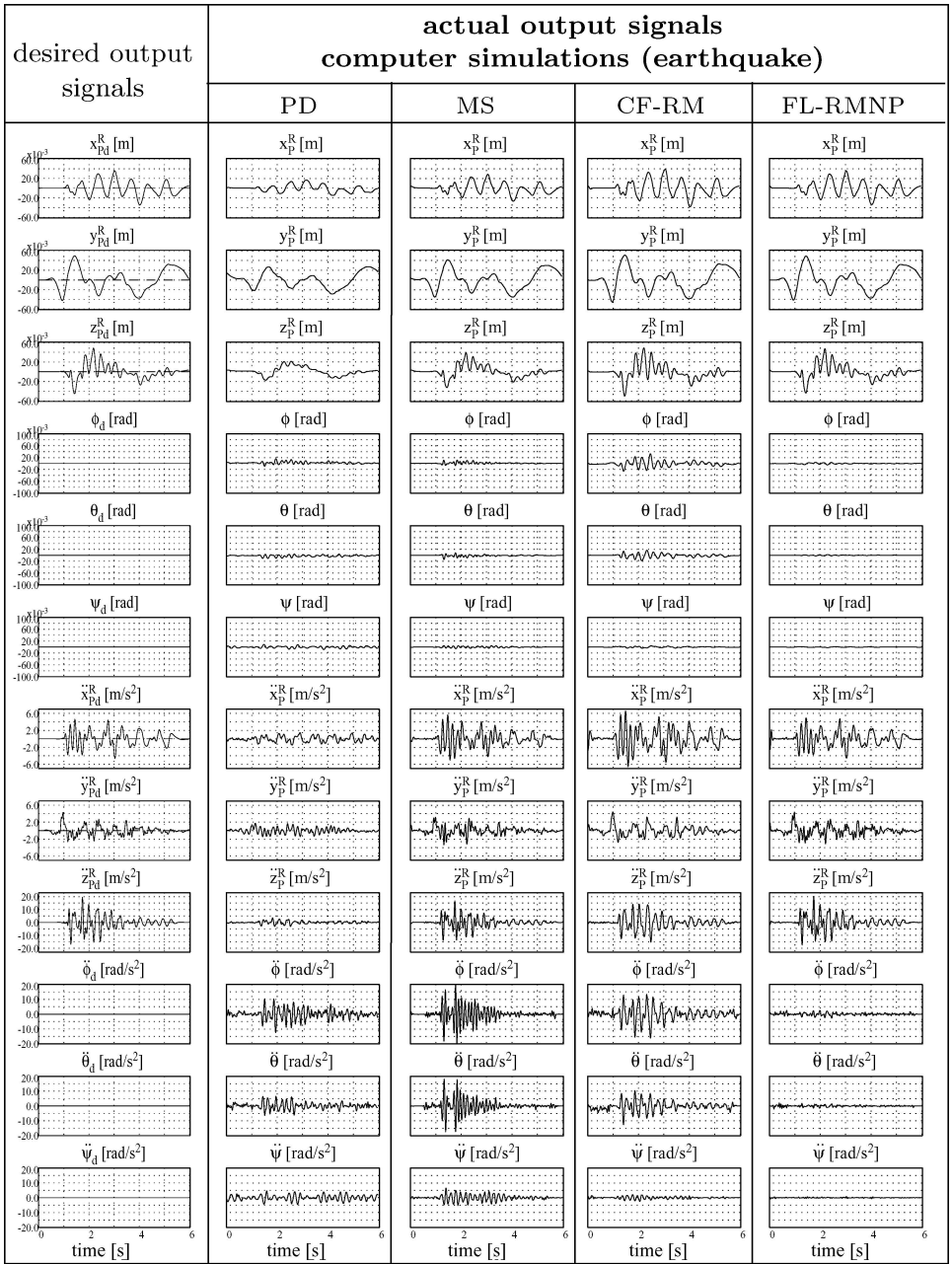

		PD	MS	CF-RM	FL-RMNP
CPU-time [ms]		0.368	0.387	0.596	0.916
control quality	q_x	26.752	72.771	53.161	301.104
	$q_{\ddot{x}}$	0.102	0.132	0.103	0.515

(a)

Figure 6. (a) Tracking and decoupling behavior due to modified earthquake signals as inputs. (b) Control errors due to modified earthquake signals as inputs.

(*Continued on next page*)

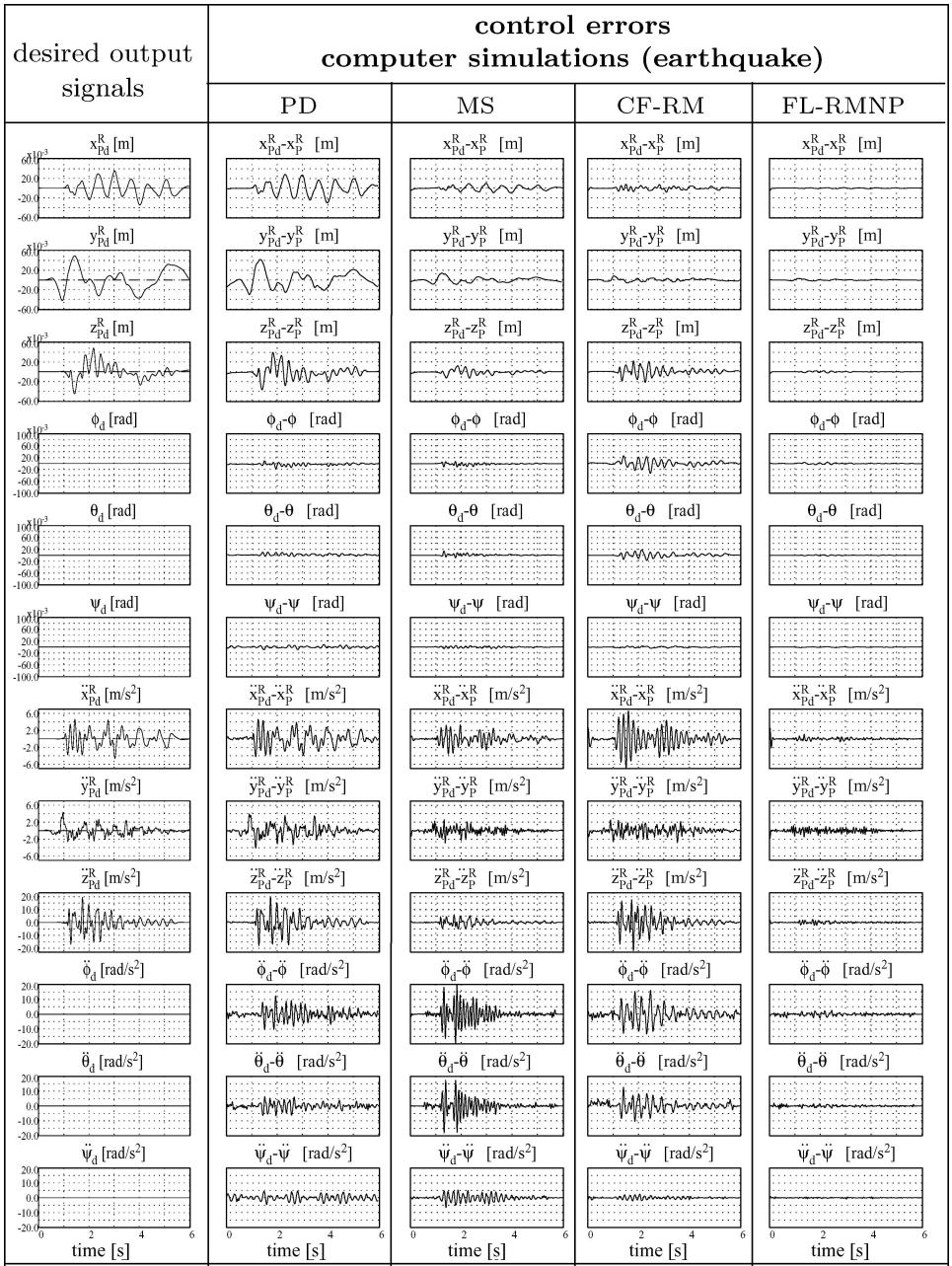

		PD	MS	CF-RM	FL-RMNP
CPU-time [ms]		0.368	0.387	0.596	0.916
control quality	q_x	26.752	72.771	53.161	301.104
	$q_{\ddot{x}}$	0.102	0.132	0.103	0.515

(b)

Figure 6. (Continued.)

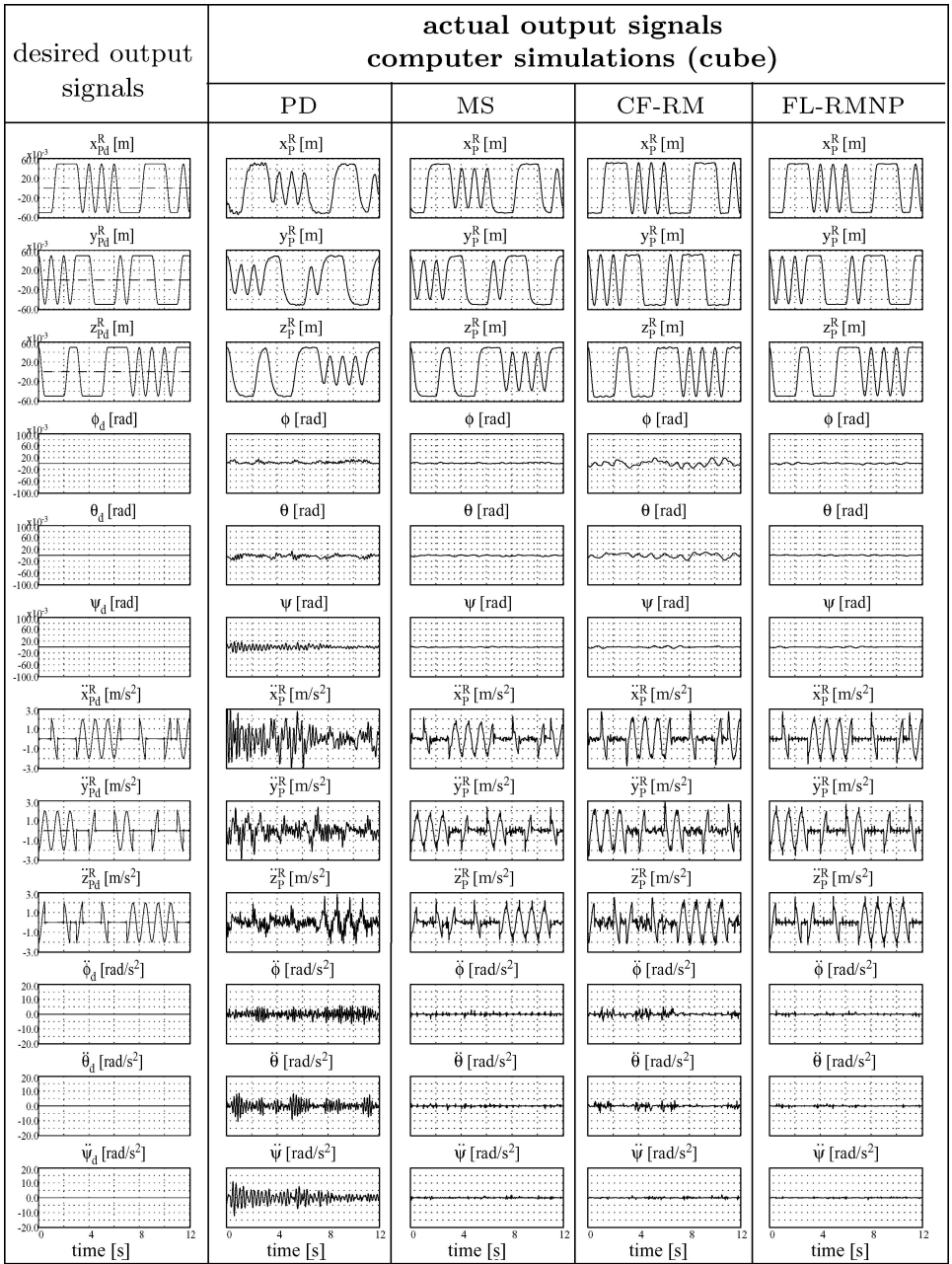

		PD	MS	CF-RM	FL-RMNP
CPU-time [ms]		0.368	0.387	0.596	0.916
control quality	q_x	7.625	23.336	22.731	95.118
	$q_{\ddot{x}}$	0.057	0.276	0.204	0.541

(a)

Figure 7. (a) Tracking and decoupling behavior for motions between the corners of a cube. (b) Control errors for motions between the corners of a cube.

(*Continued on next page*)

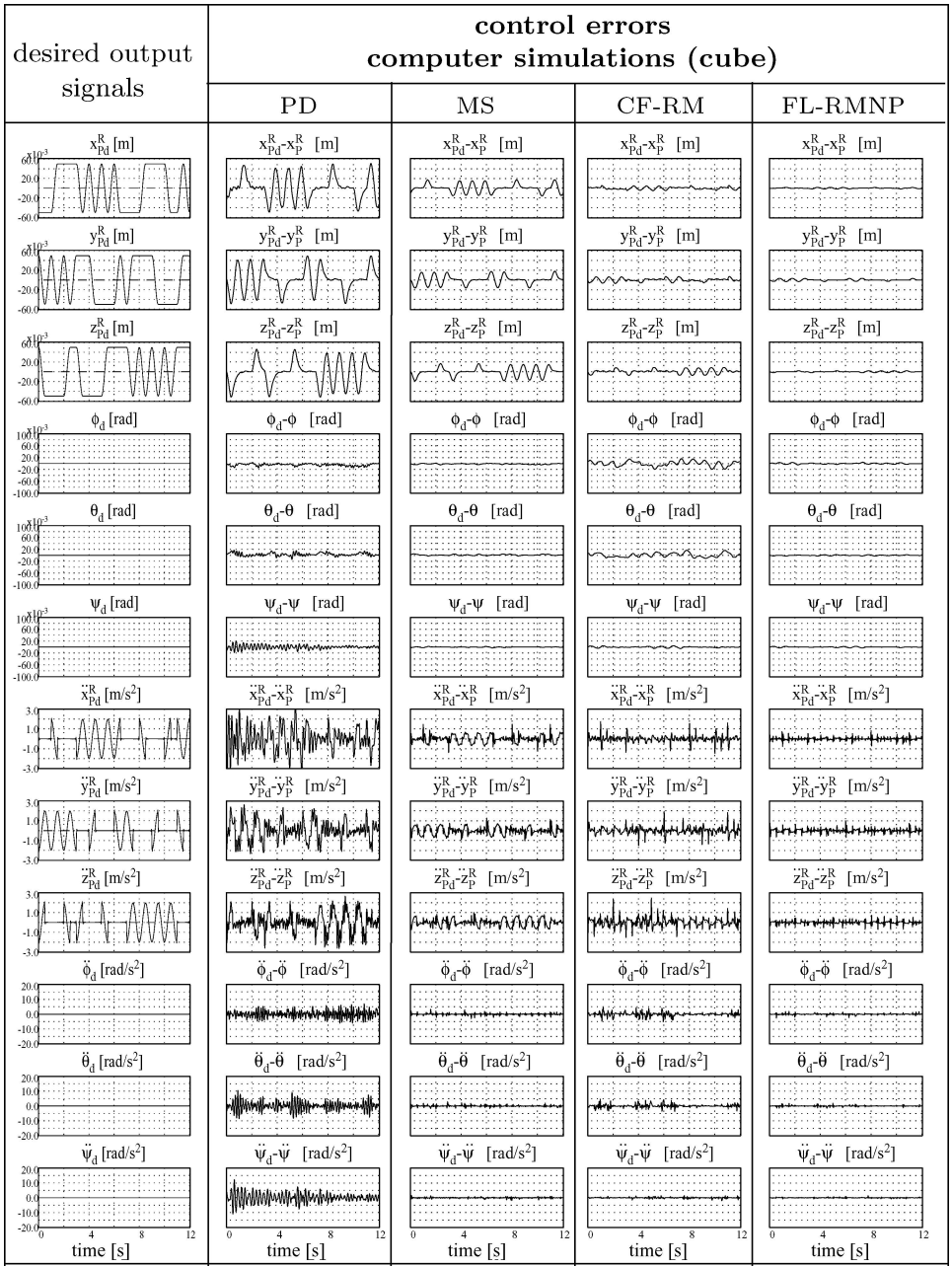

(b)

Figure 7. (Continued.)

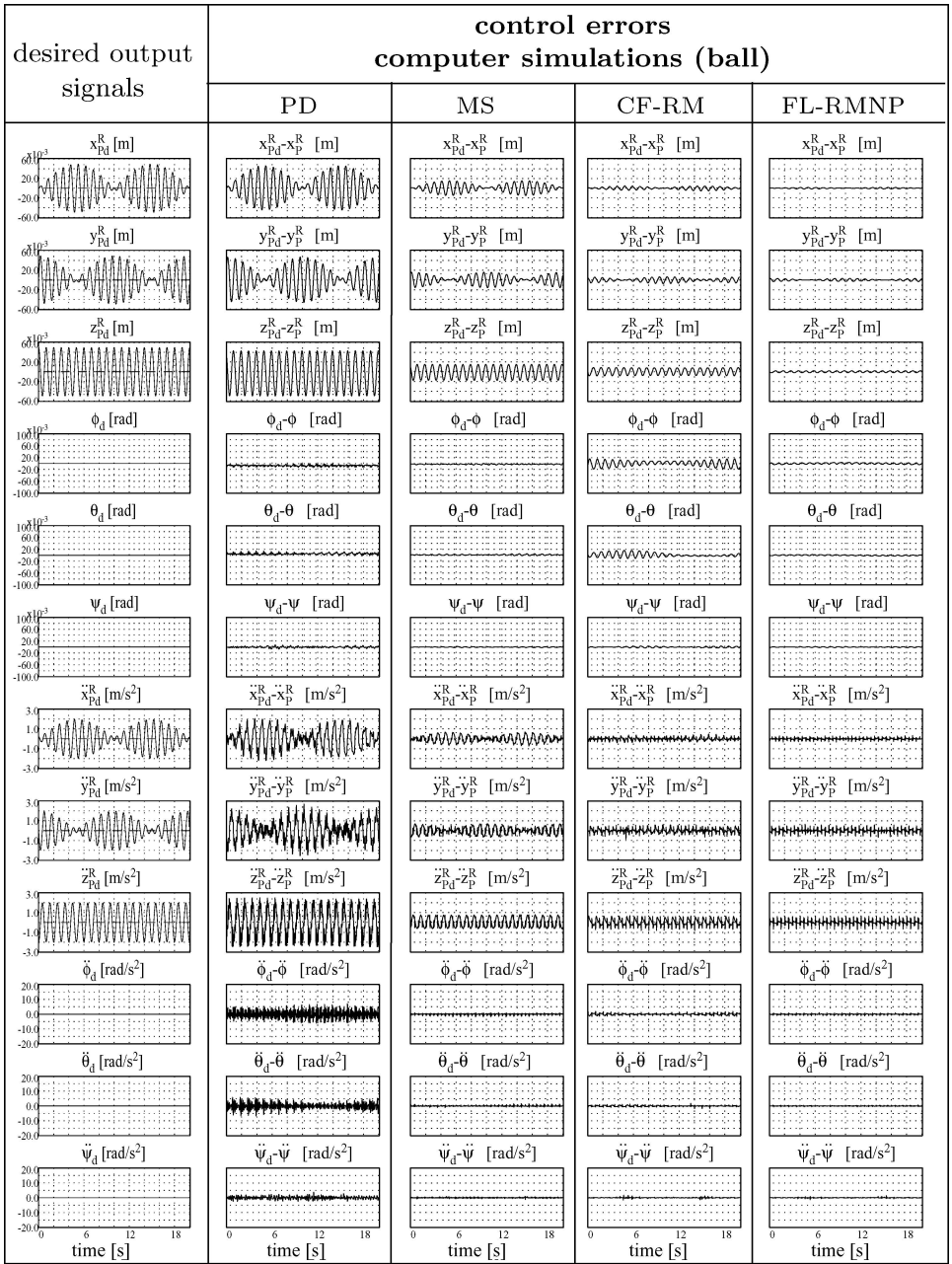

(a)

Figure 8. (a) Control errors for motions on the surface of a ball. (b) Tracking and decoupling behavior for a sine-sweep command-input signal.

(*Continued on next page*)

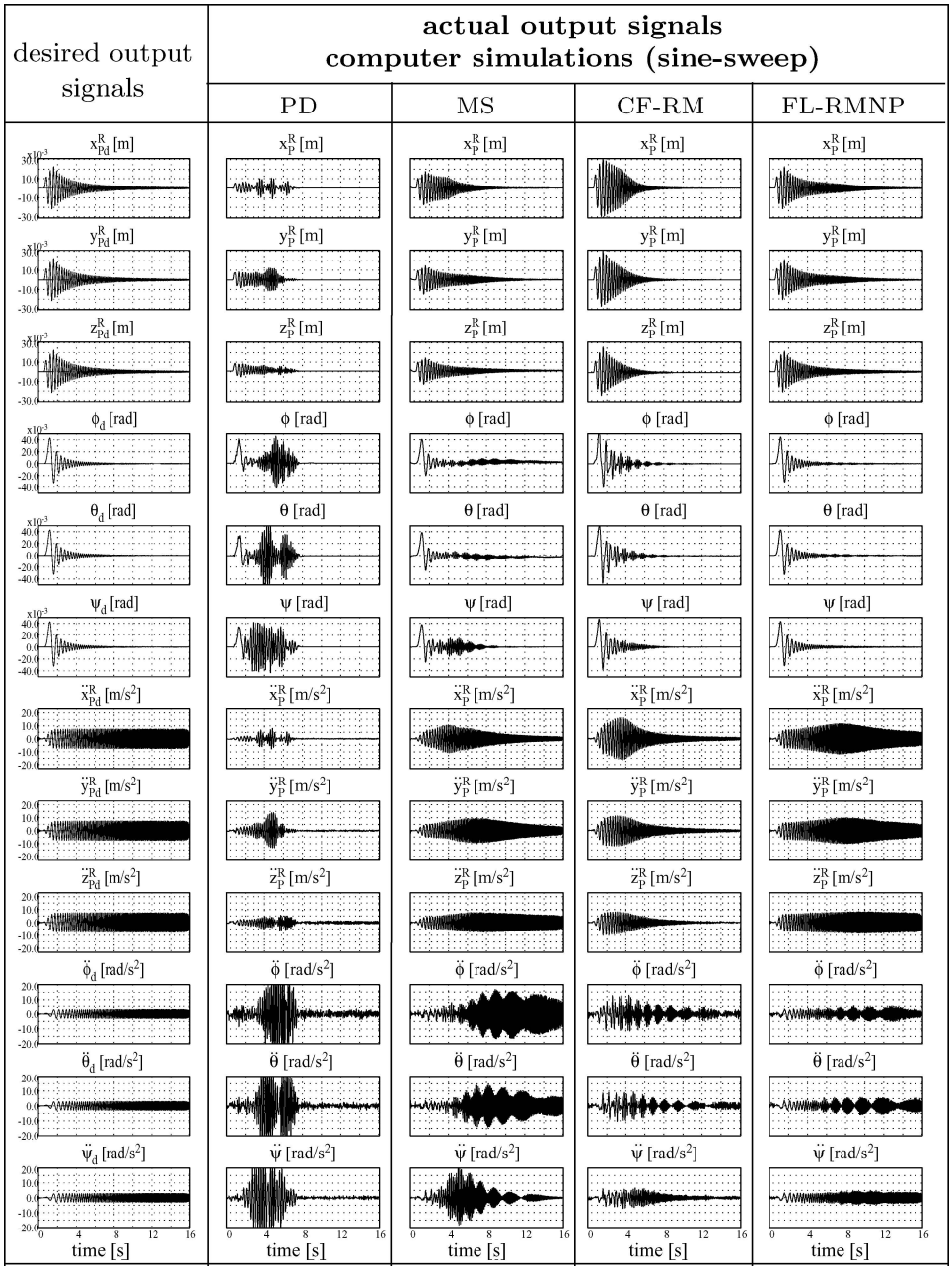

(b)

Figure 8. (Continued.)

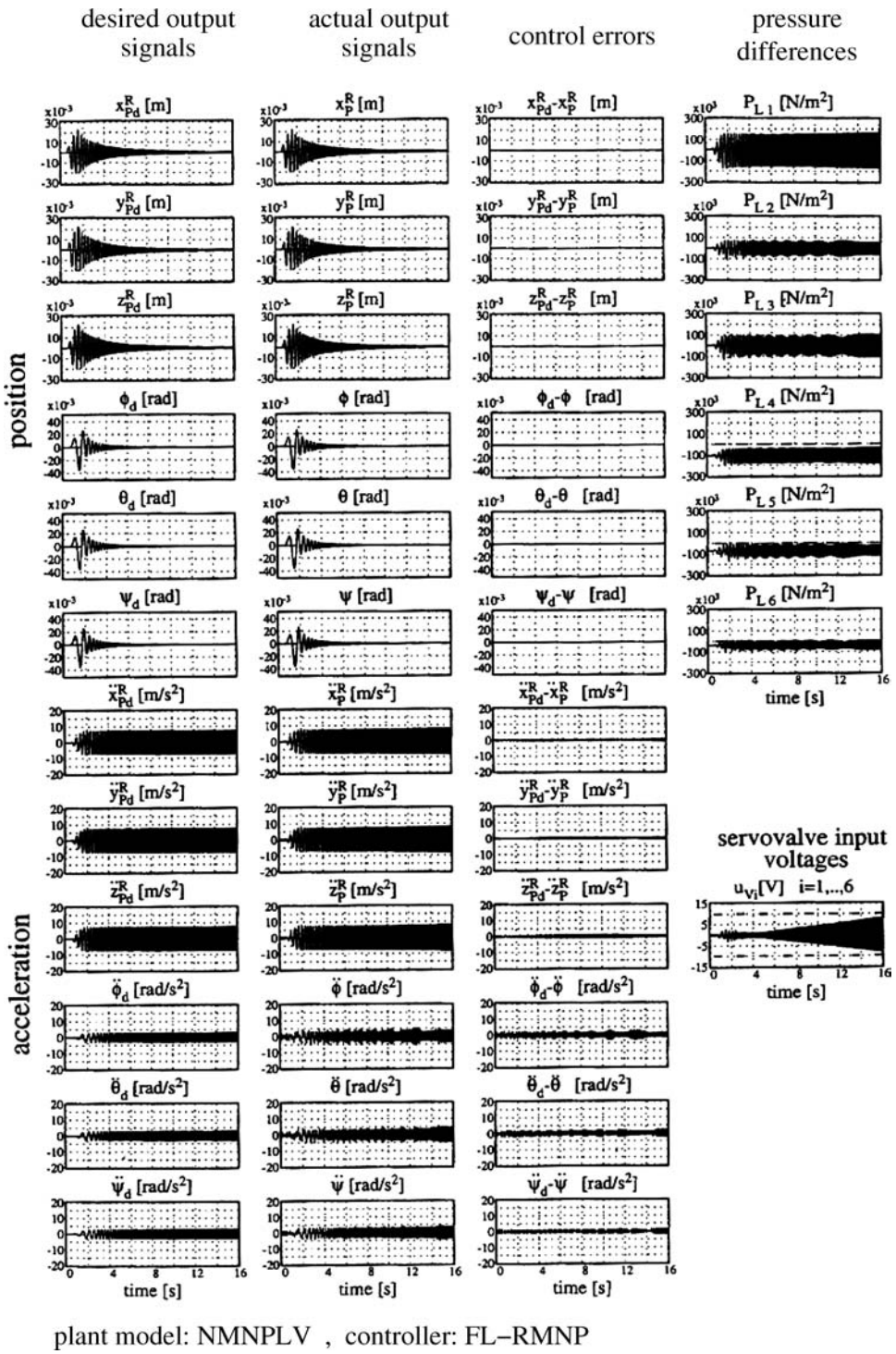

Figure 9. Improved system behavior for sine-sweep command-input signals obtained for tuned parameters of the controller FL–RMNP in computer simulations.

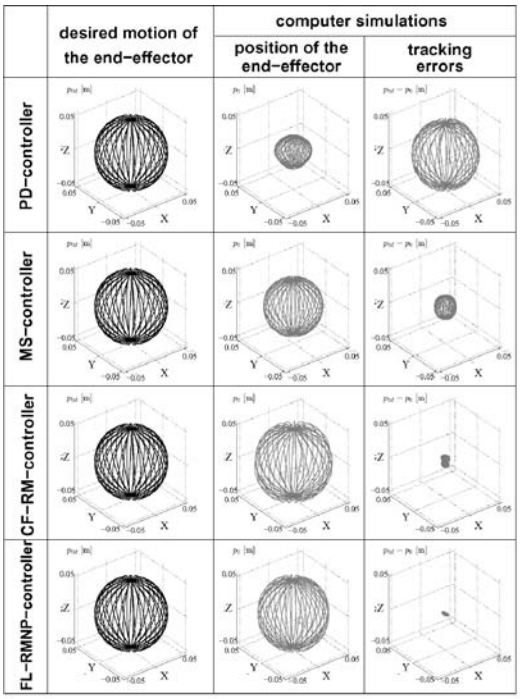

(a) Motions on the surface of a ball

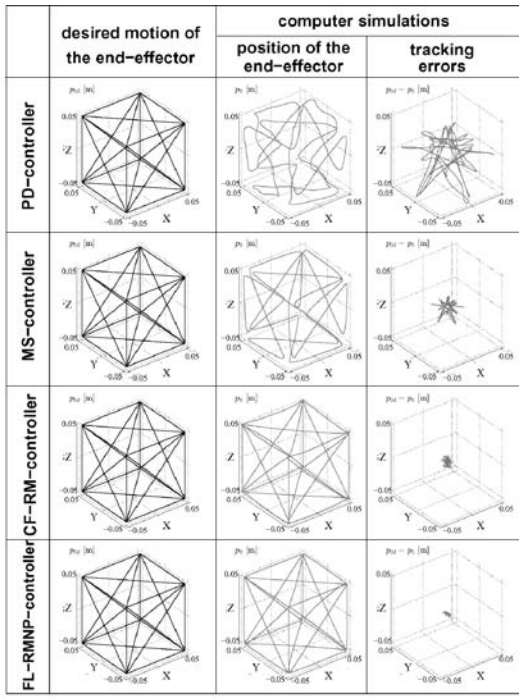

(b) Motions between the corners of a cube

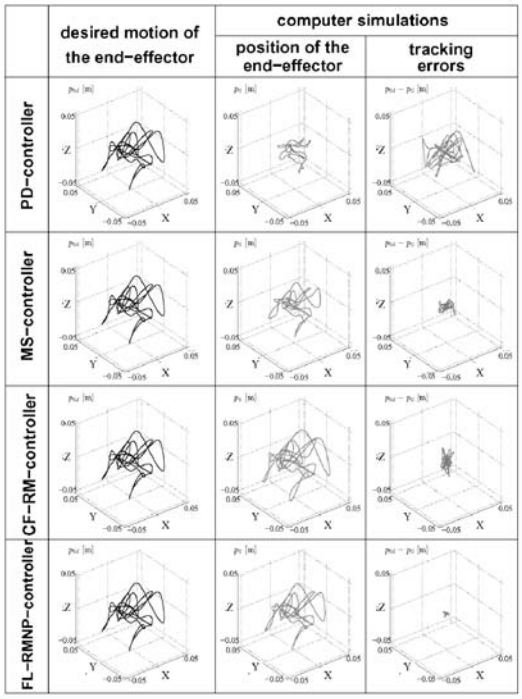

(c) Motions due to modified earthquake command-input signals

Figure 10. Spatial motions of the end effector obtained for different controllers and command-input signals.

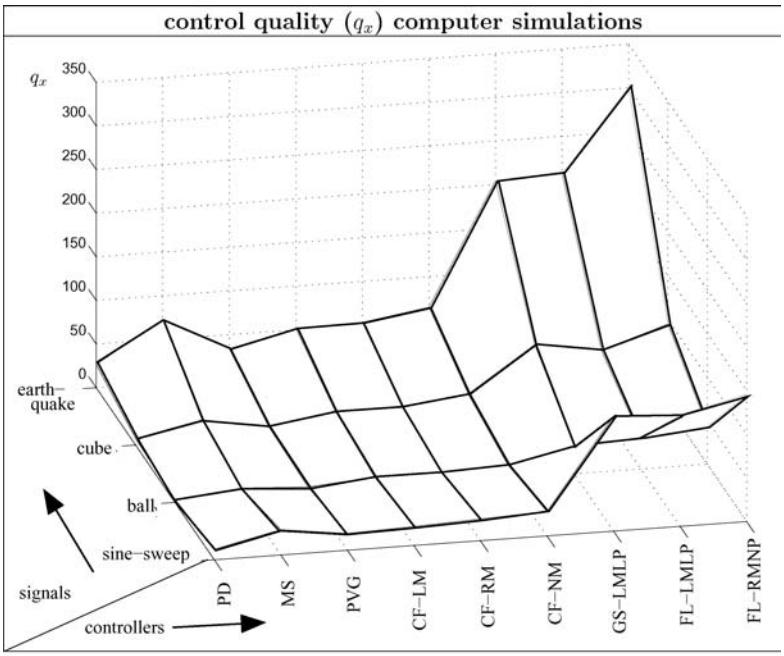

(a) Quality index q_x of the displacements

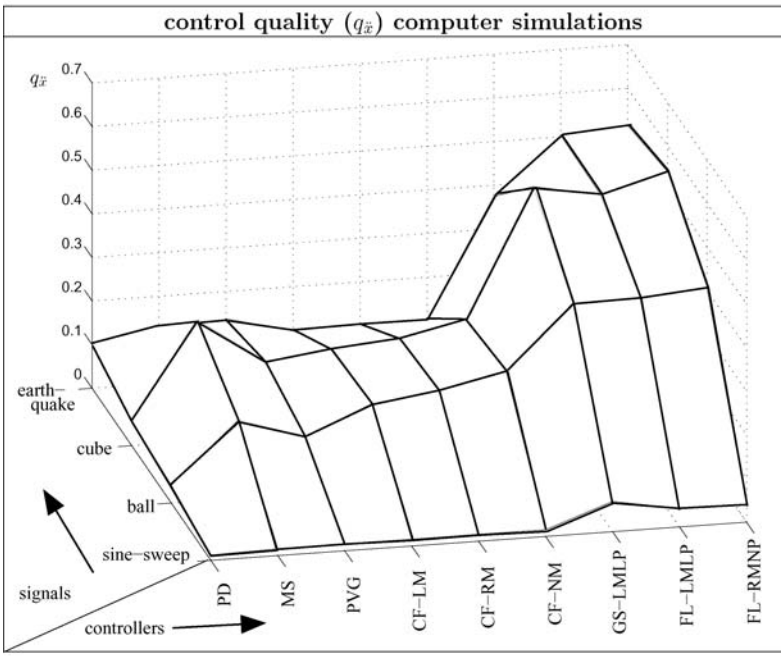

(b) Quality index $q_{\ddot{x}}$ of the accelerations

Figure 11. Quality check of the computer simulations.

with

$$\begin{aligned} \boldsymbol{x} &:= (x_{11},\ x_{12},\ x_{13},\ x_{14},\ x_{15},\ x_{16})^{\mathrm{T}} = (x_P,\ y_P,\ z_p,\ \phi,\ \theta,\ \psi)^{\mathrm{T}}, \\ \ddot{\boldsymbol{x}} &:= (\ddot{x}_{11},\ \ddot{x}_{12},\ \ddot{x}_{13},\ \ddot{x}_{14},\ \ddot{x}_{15},\ \ddot{x}_{16})^{\mathrm{T}} = (\ddot{x}_P,\ \ddot{y}_P,\ \ddot{z}_p,\ \ddot{\phi},\ \ddot{\theta},\ \ddot{\psi})^{\mathrm{T}}, \end{aligned} \tag{25c}$$

and t_{end} ($t_{\mathrm{end}} = 16$ s) as the simulation interval. The Figures 6a and 6b show the computer simulation results obtained by "modified" earthquake signals as the command-input signals (no desired rotations). These figures show that both the tracking (translational motions and accelerations) and the decoupling behavior (torsional motions and accelerations) of the test facility are stepwise improved by using controllers of increased complexity. This can be seen by direct inspection of the transient signals and by reading the quality indices. The controllers MS and CF provide results of medium quality. Only the controller FL–RMNP nearly provides ideal results. The controllers could be further improved by tuning the parameters of the linear parts of the controllers to the chosen input signal (compare the Figures 8b and 9). In the Figures 7a and b, computer simulation results are shown for motions between the corners of a cube. Again, the quality of the control loop is much better for the sophisticated controllers compared with the simpler controllers, as is seen by direct inspection of the time histories of the motions and accelerations of the test facility and by reading the quality numbers. The FL–RMNP controller provides, again, the best results, but the tracking behavior of the translational accelerations is no longer ideal, whereas the torsional DOFs are well decoupled. Such motions are commonly required in applications of parallel robots as machine tools and motion simulators. Here the time histories of the accelerations of the DOFs play a minor role compared with the trajectories of the spatial motion of the end effector or simulation platform. In Figure 8a, the simulation errors of the motion of the test table (end effector, simulation platform) on the surface of a ball are shown. The control loop provides for this motion results which are qualitatively similar to the results of Figure 7a. Sine-sweep acceleration signals in all DOFs of the test table within the frequency range from 0–16 Hz and with a frequency increase of 1 Hz/s make the highest demands on the parallel robot, as is shown in Figure 8b. Here, even the FL-controller no longer provides an ideal tracking and decoupling behavior of the accelerations of the DOFs of the test table. Here again, the system behavior can be severely improved by tuning the parameters of the linear controllers to this specific command-input signal (see Figure 9). An overview of the quality of control of the MAP obtained for different command-input signals and controllers is obtained by visual inspection of Figure 10, where the *spatial motions* and the tracking errors of the end effector are drawn. The quality of control of the robot simulations due to the different command-input signals and control algorithms is evaluated by means of the *quality indices* q_x and $q_{\ddot{x}}$ in Figure 11. These figures quantitatively confirm:

1. The quality of control obtained by conventional *PD-controllers* in combination with the *nonlinear kinematic decoupling* prefilter is poor for all types of the command-input signals used. This control concept is currently still most often used in practical applications of parallel robots.
2. The quality of control is stepwise increased by using model-based controllers of a stepwise increased complexity.
3. The different computed-force controllers (CF) only slightly improve the control system with respect to the simpler MS-and PV-controllers. This implies that the detailed information of the *kinetic behavior* of the *test facility mechanics* (gyroscopic terms, centrifugal forces, etc.) is of minor importance for the controller design of the above experiments.
4. The feedback-linearization controllers (FL) which include detailed information of both the kinematic and kinetic behavior of the test table and the pneumatic actuators provide the by far best tracking and decoupling behavior of the robot.

5. Conclusions

The essential results of this paper are that – at least in the computer simulations – modern linear and nonlinear model-based controllers may tremendously improve the dynamic behavior of a parallel robot. But this result can only be obtained if (i) both the model equations of the essential components of the robot and the model parameters are carefully derived, and (ii) if the most important properties of the model equations are included in the controllers. An unexpected result is that the computed-force controllers (CF) which include the basic kinetic properties of the test-facility do not provide much better results than the much simpler MC-controller which does not explicitly include such detailed information about the MAP. As the feedback linearization controllers (FL) provide much better results, it must be concluded that the inclusion of the actuator dynamics into the control algorithms plays a key role in these experiments. As till now the above results only hold in the virtual world of the computer simulations, *laboratory experiments* are needed in a next step, which include the same parallel robot and the same control algorithms, and which are driven by the same spatial command-input signals as the preceding computer simulations. These experiments will prove whether the computer simulations are close enough to reality such that the above results are relevant for industrial applications. In a current research project, a test stand has been built which provides answers to these practically important questions.

Acknowledgement

This work has been supported by the German Science Foundation (DFG) under Contract No. Ha 1666/6-3.

References

1. Gough, V. W. S., 'Universal tire test machine', in *Proceedings of the 9th International Technical Congress F.I.S.I.T.A.*, Vol. 117, May, 1962, pp. 117–135.
2. Stewart, D., 'A platform with six degrees of freedom', in *Proceedings of the Institution for Mechanical Engineers*, Vol. 180, No. 15, London, 1965, pp. 371–386.
3. Cappel, K., 'Motion simulator', US Patent No. 3,295,224, January 3, 1967.
4. Lebret, G., Liu, K., and Lewis, L., 'Dynamic analysis and control of a stewart platform', *Journal of Robotic Systems* **10**, 1993, 269–355.
5. Merlet, J.-P., 'Closed-form resolution of the direct kinematics of parallel manipulators using extra sensors data', in *Proceedings of the IEEE International Conference on Robotics and Automation*, Atlanta, GA, 1993, pp. 200–204.
6. Ji, A., 'Study of the effect of leg inertia in Stewart platforms', in *Proceedings of the IEEE International Conference on Robotic and Automation*, Los Alamitos, CA, 1993, pp. 121–126.
7. Raghavan, M., 'The Stewart platform of general geometry has 40 configurations', *Journal of Mechanical Design* **115**, 1993, 277–282.
8. Lee, H.-Y. and Roth, B., 'A closed-form solution of the forward displacement analysis of a class of in-parallel mechanisms', in *Proceedings of the IEEE International Conference on Robotics and Automation*, Atlanta, GA, 1993, pp. 720–724.
9. Wang, J. and Gosselin, C., 'A new approach for the dynamic analysis of parallel manipulators', *Multibody System Dynamics* **2**(3), 1998, 317–334.
10. Merlet, J., *Parallel Robots – Solid Machanics and its Applications*, Kluwer Academic Publishers, Dordrecht, The Netherlands, 2000.
11. Codourey, A., 'Dynamic modeling of parallel robots for computed-torque control', *International Journal of Robotics Research* 17(12), 1998, 1325–1336.
12. *Hexapods – a license to mill – A company claims that a concept taken from flight simulators could revolutionise machining*, in *Metalworking Production*, Vol. 139, No. 6, p. 8, 1995.

13. Ingersoll Milling Machine Company, 'Octahedral hexapod machine', *A New Technology Approach*, Rockford, IL, February 1996.
14. Hahn, H. and Raasch, W., 'Multi axis vibration test on spacecraft using hydraulic exciters', in *AGARD Conference Proceedings*, Vol. 397, pp. 23-1–23-23, Oberammergau, 1985.
15. Hahn, H., 'Mathematical modelling and simulation of multi-axes hydraulic test facilities', in *Workshop on Spacecraft Testing*, ESA SP–197, 1983, pp. 93–117.
16. Hahn, H. and Leimbach, K.-D., 'Nonlinear control and sensitivity analysis of a spatial servo-hydraulic test facility', in *Proceedings of the 32nd IEEE Conference on Decision and Control*, Vol. 2, IEEE, San Antonio, TX, December 15–17, 1993, pp. 1116–1123.
17. Fürst, D., Hahn, H., and Hecker, F., 'Mathematical modeling and parameter identification of a planar servo-pneumatic test facility. Part I: Mathematical modeling and computer simulation', *Nonlinear Dynamics* **14**, 1997, 249–268.
18. Hecker, F. and Hahn, H., 'Mathematical modeling and parameter identification of a planar servo-pneumatic test facility. Part II: Experimental identification', *Nonlinear Dynamics* **14**, 1997, 269–277.
19. Hahn, H. and Klier, W., 'Nonlinear control of a multi-axis servopneumatic test facility with redundant actuators', in *Proceedings of the International Conference on Systems, Signals, Control, Computers*, Vol. II, Durban, South Africa, 1998, pp. 461–465.
20. Hahn, H., Klier, W., and Leimbach, K.-D., 'Nonlinear control of planar parallel robots with redundant servopneumatic actuators', *Zeitschrift für angewandte Mathematik und Mechanik (ZAMM)* **79**, 1999, 79–82.
21. Neumann, M. and Hahn, H, 'Development, realization and laboratory experiments of a spatial servo-pneumatic parallel robot', in *Proceedings of the 32nd International Symposium on Robotics (ISR 2001)*, Seoul, 2001, pp. 1533–1538.
22. Klier, W., Hahn, H., and Neumann, M., 'Mathematical modeling, computer simulation and control concepts of spatial servopneumatic parallel robots', in *Proceedings of the 32nd International Symposium on Robotics (ISR 2001)*, Seoul, 2001, pp. 1719–1724.
23. Hahn, H., 'Mathematisch-physikalisches Modell eines ungeregelten elektro-servopneumatischen Antriebs', *RTS-Bericht RT-2, Fachgebiet Regelungstechnik und Systemdynamik (Maschinenbau)*, Universität-Gh Kassel, 1988.
24. Hahn, H., 'Nichtlineare Regelung eines servopneumatischen Antriebs', *Automatisierungstechnik* **48**(3), 2000, 140–150.
25. Backé, W., 'Grundlagen der Pneumatik', Technical Report, Vol. 9, Auflage, Institut für hydraulische und pneumatische Antriebe, RWTH Aachen, 1999.
26. McCloy, D. and Martin, H. R., *Control of Fluid Power*, Ellis Horwood Limited, Chichester, 1980.
27. Andersen, B. W., *The Analysis and Design of Pneumatic Systems*, Wiley, New York, 1967.
28. Hahn, H., *Rigid Body Dynamics of Mechanisms: Vol. I Theoretical Basis*, Springer, Berlin, 2002.
29. Hahn, H., *Rigid Body Dynamics of Mechanisms: Vol. II Applications*, Springer, Berlin, 2003.
30. Leith, D. W. L., 'Survey of gain-scheduling analysis and design', Technical Report, Department of Electronic and Electric Engineering, University of Strathclyde, Glasgow, UK, 1999.
31. Klier, W., 'Theoretische Modellierung, Rechnersimulation und Regelung räumlicher servopneumatischer Parallelroboter', Dissertation at RTS (Regelungstechnik und Systemdynamik, Universität Kassel), Shaker, Aachen, 2002.
32. Isidori, A., *Nonlinear Control Systems*, 3rd edn., Springer, Berlin, 1995.
33. Slotine, J.-J. E., *Applied Nonlinear Control*, Prentice-Hall, Englewood Cliffs, NJ, 1991.